Modeling the Transport and Interaction of Paperboard ”Confetti” in Pipes

by Ludvig Willemo

LUND
UNIVERSITY

Thesis for the degree of Master of Science

Company advisor: Dr. Aurélia Vallier
University advisor: Assoc. Prof. Hesameddin Fatehi

This degree project for the degree of Master of Science in Engineering has been conducted at the Division of Fluid Mechanics, Department of Energy Sciences, Faculty of Engineering, Lund University in collaboration with the Virtual Modelling team at Tetra Pak Packaging Solutions AB.

Supervisor at Tetra Pak Packaging Solutions AB was Dr. Aurélia Vallier. Supervisor at the Division of Fluid Mechanics was Associate Professor Hesameddin Fatehi. Examiner at Lund University was Researcher Robert-Zoltán Szász.

Department of Energy Sciences
Faculty of Engineering
Lund University

ISSN: <0282-1990>
LUTMDN/TMHP-24/5562-SE

Typeset in LaTeX
Lund 2024

Abstract

During the production of Tetra Pak's packaging material, holes are cut for straws and caps, generating paperboard scraps known as confetti. These scraps must be removed from the machinery to prevent build-up and potential blockages. To design efficient extraction systems, experiments and simulations are employed to understand the phenomena of confetti transport. Confetti are introduced into a simplified extraction geometry and their movement is captured using high-speed photography. The obtained data, extracted by computer vision scripting, contributes to the evaluation of joint fluid-structure interaction models simulated using the Star-CCM+ computational fluid dynamics software.

The analysis reveals that confetti transport exhibits chaotic characteristics, as seemingly identical experiments and simulations result in unique trajectories through the extraction geometry. Although the model cannot predict individual confetti trajectories, these trajectories are similar to those observed in the experiments. When evaluating the average speeds of confetti within regions of interest, the range of averages consistently increases downstream, accompanied by an increasing overestimation of velocities. This overestimation is likely due to unaccounted losses from an imperfect contact model, which also leads to identical simulations producing different outcomes. Despite its limitations, the model offers valuable insights into confetti transport and serves as a foundation for further development by Tetra Pak, supplemented by the knowledge gained from its construction.

Keywords: Fluid-structure interaction (FSI), computational fluid dynamics (CFD), finite element analysis (FEA), image analysis, paperboard, pipe debris

Acknowledgments

I extend my greatest gratitude to those who have helped me along the way, primarily my wonderful supervisors, Aurélia Vallier and Hesameddin Fatehi, for their continuous support and encouragement. Aurélia, you have always been there for discussions and guidance, and as a mentor, you have taught me a lot about being a CFD engineer. Hesam, through our weekly meetings you helped forge the thesis and your help with the writing was valuable.

To my colleagues at the Virtual Modelling department at Tetra Pak, thank you for making me feel so welcome, it has been a joy working alongside you. I would like to recognize Malin and Gustaf for our many discussions on confetti modeling, Eskil for encouragement and information sharing, Bengt for helping with experimental equipment, and Fredrik for programming inspiration and support.

Thank you, Lea Christierson, for allowing me to reuse your illustrations. Your thesis served as an excellent example and provided valuable inspiration. Additionally, I would like to express my gratitude to the Siemens support team for their assistance in resolving simulation issues and for providing academic licenses for the final set of simulations.

Lastly, I would like to thank my family for their support throughout my education and particularly during the thesis. With these words, I conclude my five-year journey towards becoming an engineer. As I leap into an exciting new world of problem-solving and learning, I thank all of you!

Ludvig Willemo
Lund, March 2024

Contents

Abstract iii

Acknowledgments v

1 Introduction 1
- 1.1 Background . . . 1
- 1.2 Previous Work . . . 2
- 1.3 Project motivation . . . 4
- 1.4 Objective . . . 5
- 1.5 Limitations . . . 5
- 1.6 Thesis Outline . . . 6

2 Theory 7
- 2.1 Background . . . 7
- 2.2 Fluid Mechanics . . . 8
  - 2.2.1 Governing equations . . . 8
  - 2.2.2 Turbulent flows . . . 9
  - 2.2.3 Turbulence Modelling . . . 10
- 2.3 Solid Mechanics . . . 12
  - 2.3.1 Governing Equations . . . 12
  - 2.3.2 Material laws . . . 13
- 2.4 Fluid-Structure interaction . . . 13
- 2.5 Computational mechanics . . . 14
  - 2.5.1 Computational Fluid Dynamics . . . 14
  - 2.5.2 Finite Element Analysis . . . 16
  - 2.5.3 Solver Coupling . . . 18

3 Experimental Set-up 21
- 3.1 Equipment . . . 21
- 3.2 Recording . . . 23
- 3.3 Computer Vision . . . 25

4 Computational Set-up 29
- 4.1 Geometry and Domain . . . 29
- 4.2 Overset . . . 30
- 4.3 Mesh . . . 31
- 4.4 Boundary Conditions . . . 33

4.5 Initial Conditions . . . 34
4.6 Models . . . 34
4.7 Solvers . . . 34

5 Results and Discussion 37
5.1 Results from Developmental Studies . . . 37
5.1.1 Flow Measurements . . . 37
5.1.2 Inlet Extension . . . 38
5.1.3 Pipe shortening . . . 41
5.1.4 Turbulence model . . . 42
5.1.5 Contact model . . . 43
5.2 Experiments . . . 44
5.2.1 Static charges . . . 45
5.2.2 Trajectories . . . 46
5.2.3 Positions . . . 49
5.2.4 Velocities . . . 50
5.3 Simulations . . . 53
5.3.1 Consistency . . . 54
5.3.2 Trajectories . . . 56
5.3.3 Positions . . . 59
5.3.4 Velocities . . . 61
5.3.5 Solver Diagnostics . . . 64
5.4 Comparison . . . 65
5.4.1 Trajectories . . . 65
5.4.2 Velocities . . . 66
5.4.3 General Observations . . . 67

6 Conclusion 69
6.1 Key Findings . . . 69
6.2 Future Work . . . 70
6.2.1 Experiments . . . 70
6.2.2 Simulations . . . 71
6.2.3 Rotary Die Cutter Model . . . 72

Bibliography 73

Appendices 75

A Populärvetenskaplig Sammanfattning 76

B Popular Science Summary 77

1 Introduction

Technological advancements in computation have allowed the field of computational mechanics to expand during the past decades, greatly aiding industries in product development by enabling studies of mechanical properties in a virtual environment. Fluid and solid mechanics are modeled by different methods, known as computational fluid dynamics (CFD) and finite element analysis (FEA) respectively. When both are combined, it results in fluid-structure interaction (FSI) models [1].

1.1 Background

Tetra Pak is a multinational food processing and packaging company of Swedish origin that is primarily known for carton packages, which they produce in billions each year. With a global goal of making food safe and accessible everywhere, Tetra Pak has continuously developed and maintained a portfolio of different packaging solutions that service different world markets [2].

Of these packaging solutions, many utilize Pre-laminated hole technology (PLH) during the production of packaging material at converting factories. There, rolls of paperboard material are: printed with customer designs, creased with fold patterns, cut to accommodate caps and straws, and laminated with layers of plastic. The finished packaging material can be used in a filling machine, in which a package is folded into its final shape and filled with the wanted product.

Rotary die cutting, illustrated by figure 1.1a, is used to perforate the paperboard as it passes between two closely mounted rollers. The resulting paperboard cut-outs are called *confetti*. These are sucked into the female dies which are connected within the roller to an extraction system, shown in figure 1.1b.

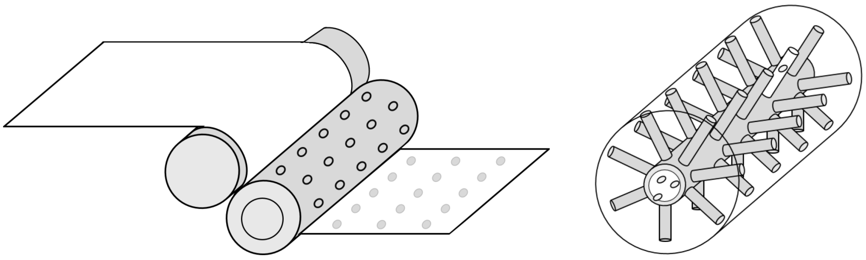

(a) Rotary die cutter. (b) Extraction system.

Figure 1.1: Illustration of rotary die cutter and its extraction system (Reprinted with permission from Lea Christierson [3]).

Depending on the confetti shape, the extraction system geometry, the amount of confetti, and the airflow conditions, the behavior and transport of confetti change drastically. From operations, three distinct traits have been observed in confetti that negatively affect the performance and reliability of the cutting process. These issues are illustrated in figure 1.2.

Both figure 1.2a and 1.2b illustrate confetti getting stuck at either joints or walls. There, confetti can accumulate, decreasing the effectiveness of the extraction and can potentially cause jams that require costly maintenance. Additionally, figure 1.2c illustrates how confetti is transported through opposite dies, possibly into the machine hall where it can interfere with the ongoing cutting process.

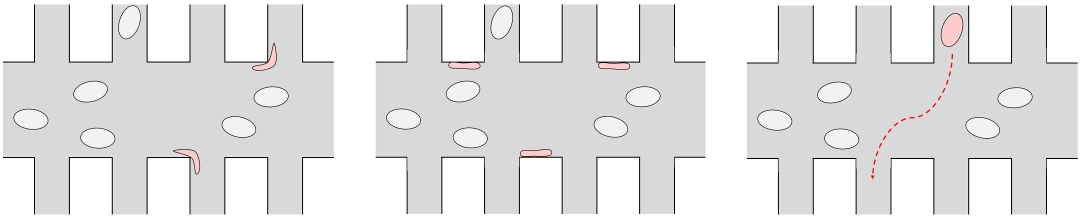

(a) Sticking to joints. (b) Sticking to walls. (c) Exit through opposite dies.

Figure 1.2: Illustration of issues observed in the extraction system (Reprinted with permission from Lea Christierson [3]).

1.2 Previous Work

To understand the behavior of the confetti during the cutting process and in the exhaust system, the virtual modeling team at Tetra Pak Packaging Solutions has developed FSI models of confetti transport. These are used to increase their understanding of confetti transport and to aid design of reliable extraction system geometries. Development in these models has been ongoing for years alongside experimental tests of modified extraction system geometries.

The first model contained one confetti in a short pipe and was set up as a co-simulation using both CFD software Star-CCM+ and FEM software Abaqus. With contributions from Lea Christierson's master thesis, it was further developed to contain two confetti within a T-junction, paired with experiments of the same configuration as seen beneath in figure 1.3 [3].

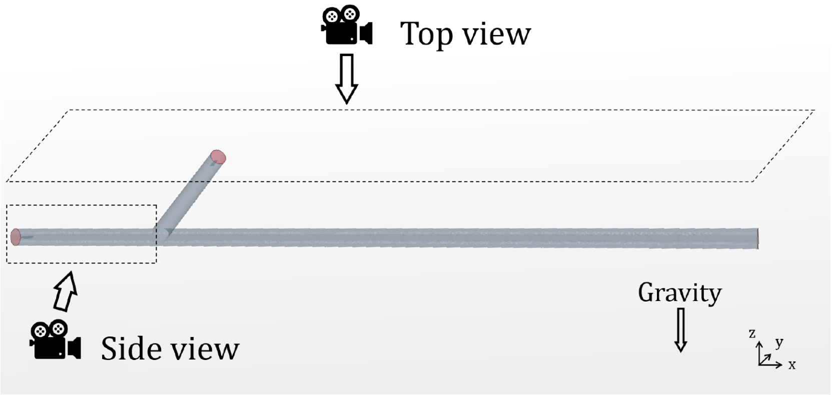

Figure 1.3: Configuration of experiments and models in Christierson's thesis (Reprinted with permission from Lea Christierson [3]).

The thesis concluded that the model could approximately capture confetti trajectories while overpredicting velocities compared to the experiments. However, no individual confetti trajectory could be predicted accurately since small changes in initial conditions, from confetti being released by hand, led to different paths as indicated in result excerpts in figure 1.4a. This indicated that confetti transport was chaotic, needing more experiments to make more certain conclusions. Trajectories from simulations are shown in figure 1.4b, illustrating the impact of different initial conditions.

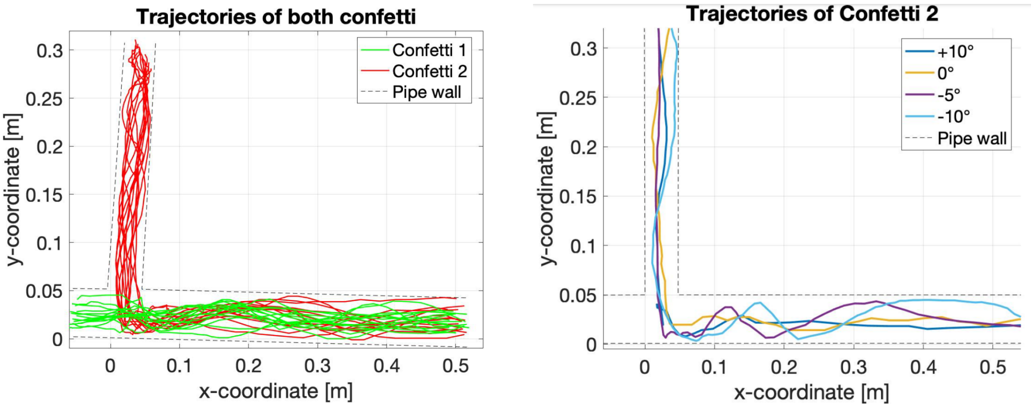

(a) Experimental confetti trajectories.

(b) Simulated confetti trajectories.

Figure 1.4: Excerpts of results from Christierson's thesis, experimental and simulated confetti trajectories (Reprinted with permission from Lea Christierson [3]).

More experiments could be gathered, but the imprecise release would limit their statistical value. The junction did not have opposing inlets, unable to capture the issues in figure 1.2c. The model being a co-simulation made them computationally time-consuming and cumbersome to configure, with unclarity whether it could be scaled to larger and more complete extraction system geometries.

1.3 Project motivation

Since Christierson's thesis, the Virtual Modelling group at Tetra Pak has worked on improving the model further. Addressing shortcomings within the experiments, a new experimental rig has been built with a release mechanism to improve the consistency of initial conditions and to allow simultaneous release of confetti. Additionally, it is coupled with new 4-way cross junctions to capture confetti entering the opposite pipes. The new rig is shown alongside camera equipment in figure 1.5.

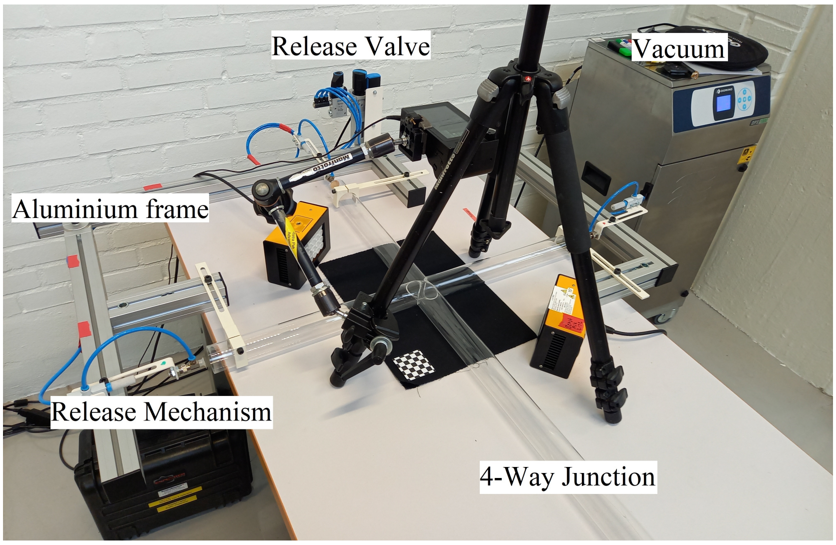

Figure 1.5: New experimental rig with annotations.

Concerning the model, new physics and features have been implemented into Star-CCM+ which should allow the model to be contained within Star-CCM+, avoiding co-simulation with a potential for sufficiently accurate and more computationally efficient results. This concept was first proven by a simplified model containing a straight pipe and one confetti, in order to assess its validity.

A new master's thesis was initiated, to utilize the advancements in a new exploration of confetti transport. Through experiments and the development of more capable models, further insight should be gained into confetti transport to further aid Tetra Pak in designing more efficient and reliable extraction systems, decreasing machine downtime and costly maintenance.

1.4 Objective

The primary objective of this thesis is to investigate the possibilities of confetti transport modeling. With the conceptual model as a foundation, new models will be constructed and refined through iterative development. In conjunction with theory, the results of each model will form the next, culminating in a final model that should replicate the new experimental rig.

In the evaluation of the final model, it should be compared against experimental data. Through this validation effort, the model accuracy will be determined. All data will be gathered through self-designed experiments where a dataset of confetti location and velocity will be extracted from high-speed footage by computer vision.

1.5 Limitations

The primary limitation was the allotted time for the thesis, which was five months (approximately twenty weeks). This was supplemented by a ten-week summer internship which allowed for familiarization with previous work and preliminary methodology exploration.

To fit within this time constraint, the scope of the model will be limited. Different packages use different material composites and opening shapes, picked for this thesis was one medium-sized circular confetti of one composite. While two cross junctions were available initially, one was destroyed during the thesis, limiting the thesis to only one orthogonal cross junction. Further, only one extraction speed was considered.

As the thesis neared its conclusion, multiple factors contributed to an undesirable limitation of only allowing one confetti in the model. This was caused by robustness issues in the final model with crashes seemingly related to confetti-confetti collisions. While weeks were spent on resolving the issue not present in previous models, the effort was unsuccessful. Contributing to the decision was that confetti-confetti collisions were not officially supported by the Star-CCM+ support team, as modules were used outside their intended usage.

The case of confetti transport through pipe junctions presents a unique challenge due to its unusual nature. The scarcity of comparable sources in the literature makes it difficult to validate models and results, the only good reference being the previous thesis by Lea Christierson. Even when expanding the scope to debris in pipes, little research applies to this case. This limits the thesis since methodology development and validation, both time-consuming activities, have to be conducted. Furthermore, the absence of peer-reviewed studies for validation could potentially compromise the reliability of the results and increase the potential for biases.

1.6 Thesis Outline

This first chapter *1. Introduction* includes a brief background that motivates the thesis subject and defines the objectives and necessary limitations. The following chapter *2. Theory*, presents the basics of fluid and structure computation, and in particular computational methods used within the final model.

Within chapters *3. Experimental set-up* and *4. Computational set-up*, the complete methodology of the thesis is presented. Each significant method choice is motivated by theory and experience from previous models. Corresponding results are presented and discussed throughout chapter *5. Results and Discussion*.

Lastly, the final chapter *6. Conclusion* summarizes key findings while addressing the thesis objectives. From this conclusion, suggestions for future research and improvements are made, concluding the thesis.

2 Theory

To understand confetti transport, there is a need to understand the fundamentals of fluid and solid mechanics, including the interaction between them. Building on this theory, modeling methods can be presented. This chapter presents relevant theory for the methods chosen in the computational set-up chapter and which are used in the final model.

2.1 Background

The junction geometry used in the experiments is a simplification of the rotary die cutter, representing the main pipe along two of its inlets as visualized in figure 2.1. Additionally, the rotation is omitted, and both the amount of confetti and the mass flow through the system are lower. In both experiments and the real machinery, the extraction of confetti is driven by airflow arising from a vacuum fan attached to the end of the system.

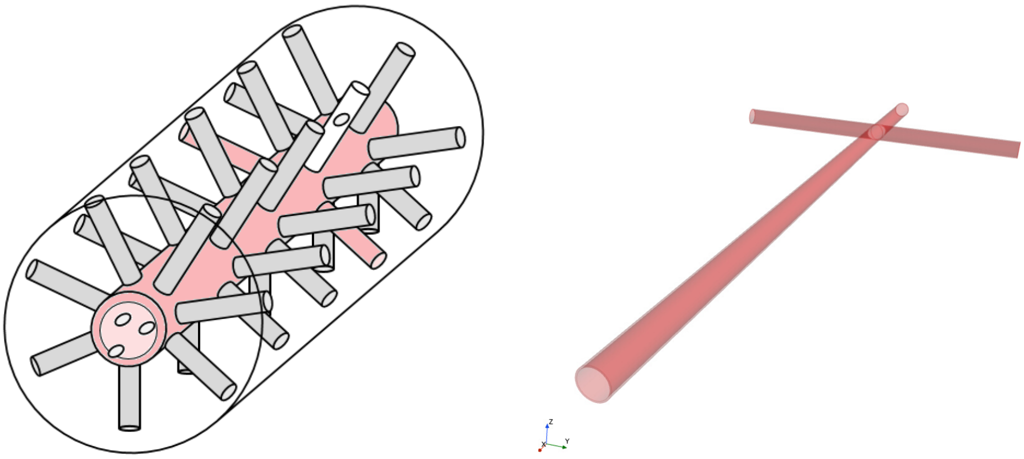

(a) Approximate real geometry.

(b) Cross junction modeled.

Figure 2.1: Illustration of simplifications made for the experimental geometry (Adapted with permission from Lea Christierson [3]).

In short, confetti and the air it is immersed in, exchange forces through fluid-structure interaction as they move relative to each other. By these forces, and those of contact with walls and gravity, the movement and deformation of confetti follows from solid mechanics. The airflow through the pipe is determined by fluid mechanics.

2.2 Fluid Mechanics

Both liquids and gases are classified as fluids, which are mediums that continuously deform and move when subjected to shearing forces. Key properties of fluids that determine their motion (fluid dynamics) are compressibility, density, and viscosity. In comparison to liquids, gases are characterized by their low density, large compressibility and ability to fill any container they are put into [4].

2.2.1 Governing equations

A mathematical description of fluid motion is constructed from conservation laws of physics, which state that a physical property must be conserved over time within an isolated system. For any fluid continuum, mass, momentum, and energy are conserved. These are formulated with differential transport equations, as equation 2.1, which conserves the generic flow variable ϕ [5].

$$\frac{\partial \phi}{\partial t} + \nabla \cdot (\mathbf{u}\phi) + \nabla \mathbf{J}_\phi = \mathbf{S}_\phi \tag{2.1}$$

The transport equation states that the rate of change of ϕ in time $\partial\phi/\partial t$ is equal to its net rate of increase due to convection $\nabla \cdot (\mathbf{u}\phi)$ and diffusion $\mathbf{J}_\phi$, and net rate of creation $\mathbf{S}_\phi$. Present variables are, time t, velocity $\mathbf{u}$, diffusive flux $\mathbf{J}_\phi$ and source term $\mathbf{S}_\phi$.

Mass conservation

Conservation of mass is guaranteed within classical mechanics. It is formulated by transfer of the density ρ, without any diffusive flux and is named the continuity equation:

$$\frac{\partial \rho}{\partial t} + \nabla \cdot (\mathbf{u}\rho) = \mathbf{S}_\rho \tag{2.2}$$

While gases are compressible, they are not always compressed. When light gases as air, flow slower than 30 % of the speed of sound, it can be assumed as incompressible with a constant density [6]. Applicable to most cases, it reduces the continuity equation to that of the equation beneath [5]:

$$\nabla \cdot \mathbf{u} = \frac{\mathbf{S}_\rho}{\rho} \tag{2.3}$$

Momentum conservation

Conservation of momentum comes from Newton's second law of motion. It states that the change in momentum of an object is equal to the sum of forces acting on it [7]. When considering a fluid continuum, the quantity transferred is density by velocity $\rho\mathbf{u}$, with diffusive flux based on the fluid stress tensor σ [5].

$$\frac{\partial\left(\rho\mathbf{u}\right)}{\partial t} + \nabla \cdot \left(\mathbf{u} \otimes \rho\mathbf{u}\right) = \nabla \cdot \sigma + \mathbf{S_u} \tag{2.4}$$

The stress tensor contains the pressure p and a viscous stress tensor τ. With air considered a Newtonian fluid, viscous stresses are proportional to the rate of deformation by the dynamic viscosity μ. Hence, the stress tensor can be written as $\sigma = -p\mathbf{I} + \mu\left(\nabla\mathbf{u} + \nabla\mathbf{u}^T\right)$. In this formulation, the stress tensor is symmetric and ensures the conservation of angular momentum [5].

Assuming both a Newtonian fluid and incompressible flow, the momentum equation is rewritten to equation 2.5. Formulated for three dimensions, it can be split into three equations commonly referred to as the Navier-Stokes equations.

$$\frac{\partial\left(\rho\mathbf{u}\right)}{\partial t} + \nabla \cdot \left(\mathbf{u} \otimes \rho\mathbf{u}\right) = -\nabla p + \nabla \cdot \mu\left(\nabla\mathbf{u} + \nabla\mathbf{u}^T\right) + \mathbf{S_u} \tag{2.5}$$

Energy Conservation

Conservation of energy comes from the first law of thermodynamics, which states that energy can only change forms and never be destroyed within an isolated system. However, for assumptions of incompressible flow and isothermal conditions, its conservation equation becomes uncoupled from the energy and continuity equations. Based on these assumptions, energy conservation is neglected by this thesis.

2.2.2 Turbulent flows

Chaotic and unstable motion within flows is called turbulence. It exhibits many unique characteristics that significantly affect most flows studied within engineering applications. Turbulent flows correspond to a high Reynolds Number, indicating that inertial forces dominate viscous forces within the fluid [6, 8].

All turbulent flows consist of rotational elements known as eddies, spanning broad sizes and time scales. The larger ones contain more energy, which through dissipation provides energy to smaller ones by an energy cascade that terminates in heat at microscopic scales. Through their motion, they significantly increase the diffusion of flow quantities by mixing [8].

Complicating the prediction of turbulent flows is that the Navier-Stokes equations have no analytical solution, requiring costly numerical computation schemes. For most flows, computations are prohibitively expensive since all eddy scales of both size and time have to be resolved to capture the flow accurately. In engineering applications, turbulence modeling is a necessity even when using high-performance computing (HPC) [5].

2.2.3 Turbulence Modelling

Within CFD, the method of directly solving the Navier-Stokes equations is known as Direct Numerical Simulation (DNS). This approach is primarily used in academic research to examine the complexities of turbulence and to assess turbulence models. Apart from DNS, two other types of models are used for engineering purposes, namely Large Eddy Simulations (LES) and Reynolds-averaged Navier-Stokes (RANS).

Large Eddy Simulations reduce the computational cost by removing smaller eddy scales by spatial and temporal filtering of the Navier-Stokes equations. The impact of filtered-out eddies on flow conditions is instead approximated by models, while larger eddy scales are still resolved numerically. While a significant reduction in cost compared to DNS, it is still costly and used restrictively in high-fidelity engineering studies [5].

RANS

Reynolds-averaged Navier-Stokes reduces the computational cost by time-averaging Navier-Stokes equations and flow variables, splitting each instantaneous variable ϕ into two components, one time-averaged $\overline{\phi}$ and one of fluctuations ϕ', as per $\phi = \overline{\phi} + \phi'$. Assuming constant density and viscosity the resulting equations become [5, 8]:

$$\frac{\partial\left(\rho\overline{\mathbf{u}}\right)}{\partial t} + \nabla\cdot\left(\overline{\mathbf{u}}\otimes\rho\overline{\mathbf{u}}\right) = -\nabla\overline{p} + \nabla\cdot\left(\mu\left(\nabla\overline{\mathbf{u}} + \nabla\overline{\mathbf{u}}^T\right) - \rho\overline{\mathbf{u}'\otimes\mathbf{u}'}\right) + \overline{\mathbf{S}_\mathbf{u}} \tag{2.6}$$

The RANS equations are not closed since fluctuating components are still present in the Reynolds stress tensor $\mathbf{R} = \overline{\mathbf{u}'\otimes\mathbf{u}'}$. To close the system of equations to obtain a solvable system, the tensor is approximated through modeling with additional transport equations.

Most common approaches utilize Boussinesq's hypothesis which states that Reynolds stresses can be approximated by the mean strain rate, turbulent kinetic energy $k = \mathrm{tr}(\mathbf{R})$ and eddy viscosity ν_t as per [5]:

$$\mathbf{R} = \overline{\mathbf{u}'\otimes\mathbf{u}'} \approx -\nu_t\left(\nabla\overline{\mathbf{u}} + \nabla\overline{\mathbf{u}}^T\right) + \frac{2}{3}k\mathbf{I} \tag{2.7}$$

The first two-equation eddy viscosity model is the k-ε model, which utilized two transport equations for turbulent kinetic energy k and its rate of dissipation $\varepsilon = \partial k / \partial t$, to construct the Reynolds stress tensor. This model, with its multiple variants, is the most commonly used RANS model for engineering purposes. An alternative is the k-ω model which replaces transport of dissipation ε, with the specific dissipation $\omega = \varepsilon / k$ [8].

SST k-ω Model

The k-ε model performs well in the free stream region with the k-ω model performing well in the near wall region, with the SST (shear stress transport) k-ω model both are combined by blending to harness their strengths. This allows for an improved free stream region while still capturing near-wall effects, such as flow separation. However, it does overpredict turbulence in stagnant and strongly accelerated regions [5, 8].

The general formulation for the k-ω turbulence model is rooted in transport of k and ω by equation 2.8 and 2.9 respectively:

$$\frac{\partial (\rho k)}{\partial t} + \nabla \cdot (\rho k \overline{\mathbf{u}}) = \nabla \cdot ((\mu + \sigma_k \mu_t) \nabla k) + P_k - \rho \beta^* f_{\beta^*} (\omega k - \omega_0 k_0) + S_k \quad (2.8)$$

$$\frac{\partial (\rho \omega)}{\partial t} + \nabla \cdot (\rho \omega \overline{\mathbf{u}}) = \nabla \cdot ((\mu + \sigma_\omega \mu_t) \nabla \omega) + P_\omega - \rho \beta f_\beta \left(\omega^2 - \omega_0^2\right) + S_\omega \quad (2.9)$$

The equations contain the mean velocity vector $\overline{\mathbf{u}}$, dynamic viscosity μ, turbulent viscosity μ_t, model coefficients β^*, σ_k and σ_ω, production terms P_k and P_ω, ambient turbulence values k_0 and ω_0, and modification factors for free-shear f_{β^*} and vortex-stretching f_β [9].

For the SST variant, two blending functions F_1 and F_2 are used to blend the model coefficients, model cross-diffusion by the production term P_ω and model turbulent viscosity per equation 2.10 through the turbulent time scale T [9].

$$\mu_t = \rho k T \quad (2.10)$$

Wall Treatment

Walls are sources of turbulence and accurate predictions of the boundary are essential for a correct flow field. To make accurate predictions, all cells at walls are evaluated for a non-dimensional wall distance y^+ defined by equation 2.11. The distance between walls and cell centers y is related to the density ρ, dynamic viscosity mu, and the friction velocity u_*. The latter is an approximation that characterizes the shear stresses at the wall [9].

$$y^+ = \frac{y \rho u_*}{\mu} \tag{2.11}$$

If low ($y^+ < 5$), the cells have a fine discretization, and the complex boundary layer can be resolved properly. If the distance is high ($y^+ > 30$), individual cells cover large parts of the boundary layer, and flow properties are instead approximated by empirically constructed wall functions. These require developed boundary layers and cannot account for adverse pressure gradients, flow separation, or high curvature. For very high y^+ values, roughly above 100, wall functions become unreliable. [5].

The two different approaches are known as low- and high-y^+ wall treatment. However, both require the mesh to be adapted to one of the approaches, for example by the addition of thin prism layer cells near walls. An alternative all-y^+ wall treatment utilizes both approaches based on an evaluation of the y^+ value, using blending for any y^+ between them [9].

2.3 Solid Mechanics

Contrary to gases, solids are characterized as incompressible mediums of high density that have a finite volume, irrespective of the container they are in. These resist deformation when subjected to loads, creating a stress distribution within the solid. With deformable bodies, the solid is treated as a continuum. The stresses act on each point within the body, displacing them and by extension the entire body. The total displacement consists of both rigid body motion and local deformations of the body [7].

2.3.1 Governing Equations

The mathematical description of continuous solids is comparable to that of fluids, relying largely on conservation laws of physics. Again, conservation for mass, momentum (linear and angular), and energy holds. With assumptions of a finite incompressible solid without heat transfer, mass conservation becomes guaranteed while energy conservation is unnecessary [9, 7].

The motion and deformation of solids under such conditions are solely reliable on momentum conservation, which by Lagrangian formulation becomes the equation of motion [9]:

$$\rho \frac{\partial^2 \mathbf{x}}{\partial t^2} - \nabla \cdot \boldsymbol{\sigma} = \mathbf{f}_b \tag{2.12}$$

It relates the displacement vector $\mathbf{x}$ to the stress tensor $\boldsymbol{\sigma}$, with additional body forces $\mathbf{f}_b$. The latter contains multiple components coming from gravitational acceleration, contact methods, and momentum exchange with surrounding fluids.

2.3.2 Material laws

To obtain a solvable equation of motion, a constitutive relation is used to relate stress with strain. Each material has different deformation properties, resulting in different stress-strain curves which can be modeled to account for temporary (elastic) and permanent (plastic) deformations, and possibly fracture [10, 7].

When considering small deformations, most materials can be assumed as linear elastic. That is, stress and strain have a linear relation known as Hooke's law [10]. Its one-dimensional formulation states that stress is proportional to strain by Young's modulus E, a resistance to deformation[7]:

$$\sigma = E\varepsilon \tag{2.13}$$

If a three-dimensional material is assumed to have the same elastic response in all directions, it is isotropic. Additionally, each deformation in one direction results in deformations in perpendicular directions. The direction and magnitude of those deformations are described by the Poisson's ratio ν, used in Hooke's law for an isotropic linear elastic solid in three dimensions [7]:

$$\boldsymbol{\epsilon} = -\frac{\nu}{E}(\mathrm{tr}\boldsymbol{\sigma})\mathbf{I} + \frac{1+\nu}{E}\boldsymbol{\sigma} \tag{2.14}$$

2.4 Fluid-Structure interaction

Any object immersed in flowing fluids is affected by forces, resulting from pressure and shear stress distributions acting on its surface. Their presence is described by the momentum theorem which states: Flow which encounters an obstruction or immersed body, has its fluid particles deflected corresponding to a change in the fluid momentum. Per Newton's second law of motion, the rate of change in the fluid momentum is equal to a force acting upon it. This force must have an equal and opposite force acting on the body per Newton's third law of motion [6].

The equal and opposite force represents a transfer of momentum between fluids and structures immersed within them. When there is a significant exchange between both mediums, the interaction is described by a two-way coupled model. In some cases, for example, during the transport of small particles, the momentum transfer from the solid to the fluid might be insignificant. Then, one-way coupled interaction is assumed sufficient. With confetti being large in relation to the pipe diameter and with nonnegligible weight in comparison to air, it is assumed that two-way coupling is needed for an accurate description of the fluid-structure interactions present in confetti transport [1].

It is modeled by including these equal and opposite forces in the equations for the conservation of momentum. For the solid it is part of the body force $\mathbf{f}_b$ from the equation of motion (2.12), and for the fluid it is a part of the source term $\mathbf{S_u}$ from the RANS equations (2.6) [9, 1].

2.5 Computational mechanics

Computational mechanics is an interdisciplinary field that combines mechanics with scientific computing. It is a powerful tool used by engineers to simulate a wide range of mechanical systems with well-controlled conditions, in a virtual environment. This makes it a valuable tool for exploring the behavior of systems under different scenarios, optimizing designs, and making predictions about future behavior [10, 5].

With significant differences in solid and fluid mechanics, each requires different methods to be modeled. Finite element analysis (FEA) is used for solids, while computational fluid dynamics (CFD) is most commonly used for fluids. In some cases, these are coupled to model mechanics with fluid-structure interaction. While the computation of solids and fluids differ, they share an overall structure [11, 5]:

The creation of a computational domain is the first step of any simulation. A real-world geometry is replicated digitally and possibly in a simplified manner. Then, the domain is discretized into many elements or cells which together form a mesh. This process transforms the continuous problem into a discrete one, enabling the use of numerical methods.

Physical properties, such as pressures, loads, density, viscosity, and elasticity, are assigned to the mediums and boundaries of the domain. These properties, together with discrete formulations of the governing equations, describe the behavior of the system. By going through each element in the mesh, an algebraic system of equations is assembled.

The assembled system is then computed using mathematically robust solvers and algorithms. These solve the system of equations, providing a numerical approximation of the system's behavior. Through post-processing of the solved system, its physical properties can be visualized and more easily inspected.

2.5.1 Computational Fluid Dynamics

The finite volume method is another numerical technique used for the discretization and approximation of solutions to partial differential equations. It utilizes finite control volumes (cells) with variables stored at the centroid of each volume. Governing equations (2.3, 2.6, 2.8 and 2.9) are evaluated for conservation within each cell using Gauss divergence theorem, formulating a finite volume description of the problem [5].

Motion

The computational domain for the fluid has a hole for the confetti, which must be moved alongside the confetti motion. Commonly, this is done by using mesh morphing methods, which adapt the computational mesh to accommodate the changing shape of the fluid domain [9]. This is sufficient for most fluid-structure interaction cases of structures with limited movement. However, with free motion for the confetti, the morphing would eventually result in a heavily skewed mesh of poor quality.

Two approaches are used to avoid this issue. The first is general re-meshing, in which a new mesh is created when the original becomes too skewed. The second is the use of an overset mesh, a mesh attached to the moving structure with small morphing for local deformations overlaid on a static background mesh [12, 9]. Both were used during development, but the overset approach was ultimately chosen and will hence be presented in more detail, aided by figure 2.2.

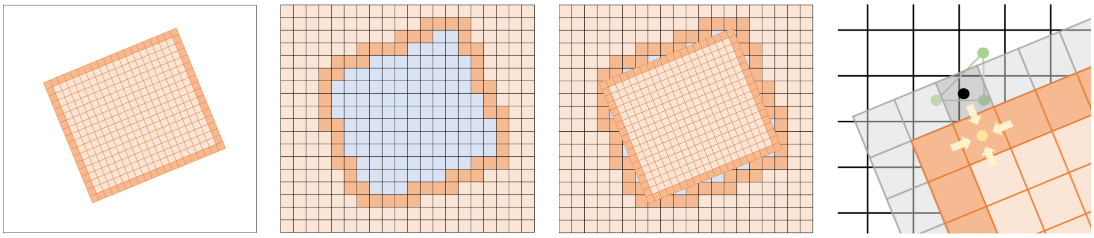
(a) Overset mesh. (b) Background mesh. (c) Overlaid meshes. (d) Cell interpolation.

Figure 2.2: Illustrations of an overset methodology with cell markings. Blue cells are inactive, light orange cells are active, and dark orange cells are acceptor cells. Dots represent cell centers and gray cells are ghost cells.(Reprinted with permission from Lea Christierson [3]).

The first step in an overset approach is to discretize the entire fluid domain into a static background mesh, see figure 2.2b. The overset mesh is created around the confetti, see figure 2.2a. It has an internal boundary towards the confetti and one facing outwards to the fluid. The latter is used to couple fluid domains of the overset and background.

A hole-cutting process is used to mark cells as active (light orange), inactive (blue), or as an acceptor (dark orange). For the overset mesh of figure 2.2a, the outermost cells are marked as acceptor cells, with active cells within them. For the background mesh of figure 2.2b, cells that are underneath the overset mesh are temporarily inactivated. Neighboring cells that enclose the inactive region, trailing the overset edge, are marked as acceptor cells. All other cells within the two meshes default to regular, active cells. Overlaid on each other, the full mesh becomes that of figure 2.2.

Flow quantities of each cell are evaluated and calculated with information from neighboring cells. In the case of acceptor cells, neighboring cells are either inactive or not there. Assumed in their place are ghost cells, marked as gray in figure 2.2d, in which flow quantities are expressed by interpolation of overlaid cells in the opposing mesh. For instance, properties stored in the ghost cell center of the overset mesh, the black dot in the illustration, are interpolated in three green cell centers of the background mesh. This method couples the two meshes, and effectively forms a unified fluid domain in which flow properties of both meshes are solved simultaneously [12, 9].

Solver

When the finite volume discretization of the governing equations is evaluated for each cell in the fluid domain, a non-linear algebraic system of equations is assembled. The solution variables are velocity and pressure, but due to the incompressible assumption, the two variables are uncoupled and segregated [5, 9].

A segregated flow solver overcomes the segregation by using the pressure-correction equation which relates the two variables. The still non-linear system of equations is solved by an iterative predictor-corrector algorithm. In this thesis, the Semi-implicit method for pressure-linked equations consistent (SIMPLEC) was used. In it, an initial guess of pressure is used to solve momentum equations for velocities. Put into the pressure-correction equation, both velocities and pressures are corrected. If these do not fulfill mass conservation or convergence, a new iteration begins from the momentum equations.

The segregated solver is used to achieve a solution for each instance in time and is paired with a time-stepping scheme to achieve a transient solution. This thesis used second-order implicit scheme, with an adaptive time step decided by a target displacement criterion for the confetti. To accelerate overall convergence, algorithmic multigrid methods are used with a Gauss-Seidel relaxation scheme. Additionally, Rhie-Chow momentum interpolation is used to avoid odd-even oscillations in the solutions [5].

2.5.2 Finite Element Analysis

The finite element method is a numerical technique that is used to discretize and approximate solutions to partial differential equations. It uses finite elements with variables stored at each element node, with the solution between them approximated by polynomials [11]. The finite element formulation for the equation of motion is presented in equation 2.15 [9, 10].

$$\mathbf{M}\ddot{\mathbf{x}} + \mathbf{f}_{int}(\mathbf{x}) = \mathbf{f}_{ext} \tag{2.15}$$

The equation describes an equilibrium of internal and external forces within the system, by a non-linear algebraic formulation. In it, $\mathbf{M}$ represents the mass matrix, $\ddot{\mathbf{x}}$ is the acceleration vector, $\mathbf{f}_{int}(\mathbf{x})$ is the internal force vector which is a function of the displacement vector $\mathbf{x}$, and $\mathbf{f}_{ext}$ is the external force vector.

To derive this equation requires many steps, summarily explained here. The equation of motion (2.12) is multiplied by a weight function and integrated over the element volume. Then by Gauss divergence theorem, it is split for each boundary to achieve the weak formulation of the equation. Assuming a weight function and polynomial approximation, a finite element formulation is obtained. As a final step, the internal force is converted from a function of stresses to one of displacements, by using the constitutive relation of equation 2.14 [10, 11].

Contact

The confetti will experience contact with the rigid pipe surface as it moves through the pipe. To replicate the physical constraint that contact imposes on the confetti, a penalty method for contact enforcement is used. It penalizes the confetti with a contact pressure, acting as an external force through $\mathbf{f}_{ext}$ in equation 2.15.

The contact pressure P is only active when the contact gap g, the distance from the solid to the rigid surface, is less than zero and indicates a penetration of the rigid surface. Then, the contact pressure is proportional to the penetration distance by the contact penalty stiffness ϵ. This corresponds to the function in equation 2.16 [9].

$$P(g) = \begin{cases} \epsilon g & , g < 0 \\ 0 & , g \geq 0 \end{cases} \tag{2.16}$$

However, penetration is an unwanted feature as it potentially breaks computational domains. By a contact gap offset parameter, the rigid surface can be offset, creating a new virtual rigid surface, to which the contact gap is calculated. Additionally, it is recommended that the contact penalty stiffness ϵ is related to the solids Young's elastic modulus E divided by the cell base size.

Solver

The finite element formulation of the equation of motion in equation 2.15 contains both a time derivative (acceleration) and is non-linear. To solve it, a time integration method is needed to relate the acceleration to displacements, converting the system into a static equilibrium equation. One such method is the implicit, unconditionally stable, and second-order accurate generalized-α method [10].

A general representation of the non-linear static equilibrium equation can be written as equation 2.17. It has a stiffness matrix $\mathbf{K}(\mathbf{x})$ dependent on the displacement vector $\mathbf{x}$. It is used to define a residual $\mathbf{r}(\mathbf{x})$ which should be minimized.

$$\mathbf{K}(\mathbf{x})\,\mathbf{x} = \mathbf{f}_{ext} \Rightarrow \mathbf{r}(\mathbf{x}) = \mathbf{K}(\mathbf{x})\,\mathbf{x} - \mathbf{f}_{ext} \tag{2.17}$$

The Newton-Raphson root-finding algorithm can solve this system. The method starts with an initial guess for the displacement vector, resulting in a residual which together with a tangential stiffness matrix, forms a new guess for the displacement vector. Repeated multiple times, the displacements vector approximates the solution [10]. The algorithm is stopped after a maximum number of iterations or when a convergence criterion is met for the residual [9].

When more complex materials are considered, with non-linear elastic and plastic traits, external loads are incrementally added over several load steps, each with multiple Newton-Raphson iterations [10, 9].

2.5.3 Solver Coupling

With a two-way fluid-structure interaction problem, the two solvers must be coupled for the exchange of momentum. The strongest coupling is available with a monolithic scheme, which combines both mediums into a single system of equations and solves both domains simultaneously [13]. However, when using two different discretizations, finite element, and finite volume, a monolithic scheme is not optimal and hence is not used [9].

The alternative is a weaker coupled partitioned solver scheme. It solves each domain separately with an additional step for the exchange of momentum. For a two-way coupled solver, this is done by iterations over a linear solver sequence for each time step. The sequence consists of a momentum exchange, followed by the solving of the solid, and afterward of the fluid. Iterations are made until the convergence criterion is met for both domains and their coupling [13, 1, 9].

When put in relation to time-stepping, the complete solver scheme becomes that of figure 2.3 [9]. It begins by initializing the solvers with a specified solution. By each time step, the time stepping size is calculated by the adaptive time-stepping method and iterations are performed as above. If converged, the time advancement is finalized by updating the solution and moving the meshes correspondingly. If the stopping time is surpassed, the solver is terminated. Otherwise, another time step is made.

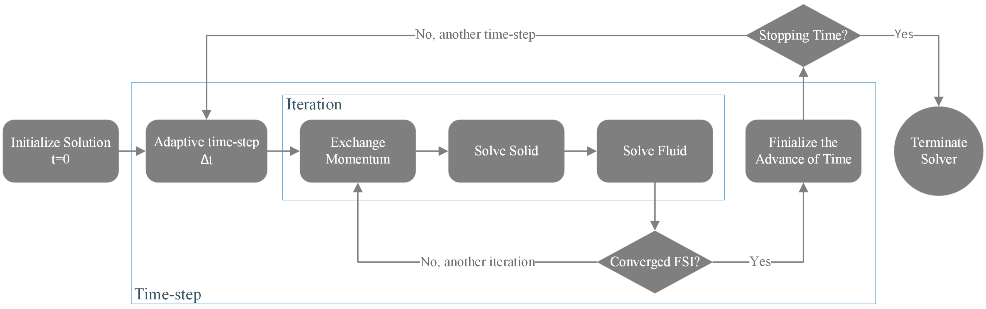

Figure 2.3: Two-way fluid-structure interaction solver scheme of this thesis.

3 Experimental Set-up

Validation is an essential part of using CFD, as computational models do not necessarily produce an accurate representation of the physical phenomena being simulated. Data used for validation will in this case come from self-performed experiments. This chapter covers the experimental set-up previously shown in figure 1.5, used to obtain the data which by itself can provide further insight into confetti behavior.

3.1 Equipment

As mentioned, development at Tetra Pak has led to a new testing rig. It is an aluminum construction with adjustable mounting brackets for different plexiglass junctions. The previous T-junction studied in Christierson's thesis, referenced in figure 1.3, is replaced with a new orthogonal four-way junction [3]. It is chosen for the possibility of capturing when confetti passes from one arm into an opposite arm. The junction is built as per the construction drawing in figure 3.1 and consists of four joined acrylic see-through pipes. These have an inner and outer diameter of 22.5 mm and 25 mm respectively. Each inlet arm spans 425 mm, with the outlet spanning 1475 mm from the junction center point.

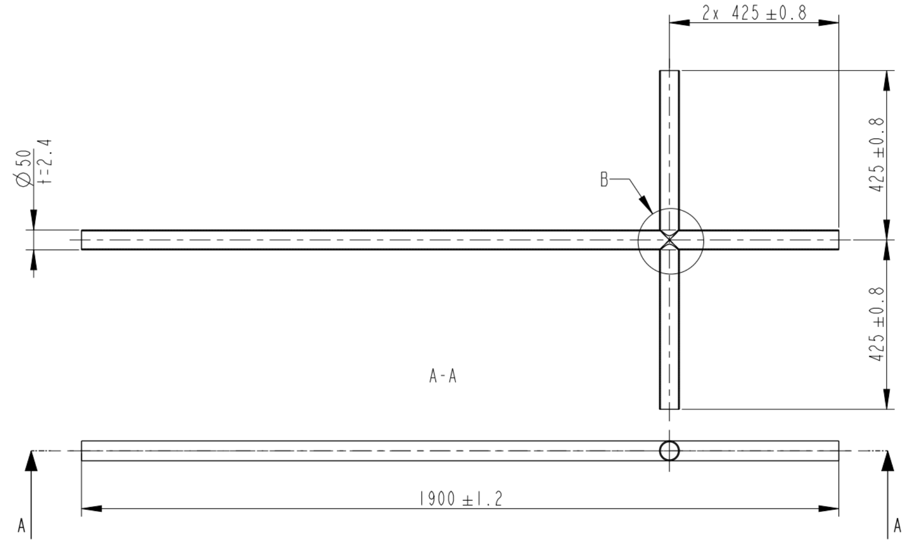

Figure 3.1: Drawing of orthogonal four-way junction with measurements. Extracted from internal Tetra Pak drawing number 3630657.

Limited to one confetti type, medium-sized circular confetti was sourced from bins at testing facilities. Having passed through an extraction system already, most were nagged at the edges. All had a diameter of 25 mm and varying sub-millimeter thickness which could not be measured accurately.

Addressing previous concerns about the confetti being released imprecisely by hand, the rig is accompanied by a pneumatic release system. It uses three suction cups for confetti staging and synchronous release by a manual valve. These were mounted for confetti to be released parallel and centered to the inlets, one centimeter in front of it.

For high-speed photography, a monochrome high-speed camera was used. For our purposes, a relatively high resolution is required to capture and post-process confetti transport. At a resolution of 1024 by 768 pixels, the camera was capable of capturing grayscale footage at a rate of 1771.2 frames per second. To operate under these conditions, this camera requires a lot of light. Hence, two powerful lamps were used to illuminate the junction with a combined output of 28,000 lumens.

These lamps constitute the only considerable risk factor as they were marked for photobiological warnings. By exposure to both direct and indirect light at short distances, the lamps have the potential to cause irritation or damage to both skin and eyes. To avert and limit exposure, the entire set-up is covered by a dark fabric and lights are turned off when not in use. However, the lights have significant heat output which could pose a fire hazard. To avert this new risk, participants were notified of the location of a nearby fire extinguisher.

A fume vacuum system is used to drive the flow by a flexible tube attached to the junction outlet. Due to the set limitations, the adjustable target extraction speed is set to its lowest at 10 m/s. However, there were two issues with this. One is that the speed on its display indicated varying velocities. Two, with unknown pass-through areas for the velocity, it is impossible to extract necessary mass flow conditions at the outlet.

Addressing these two concerns, speed was measured at the outlet to quantify variations in flow conditions. For measurements, an anemometer was used with a 60 mm diameter propeller probe. To obtain the most accurate results, the probe was inserted between the junction outlet and tube intake. Any gaps were covered with tape to reduce escaping mass flow. The resulting set-up is shown beneath in figure 3.2.

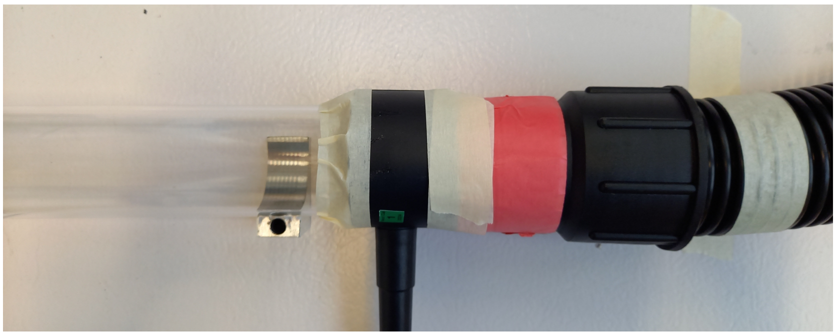

Figure 3.2: Anemometer placement for speed measurements. Acrylic junction outlet (left), black anemometer probe (middle), flexible vacuum tube (right).

3.2 Recording

The methodology used when recording was influenced by the development of computer vision scripting which benefited heavily from clear contrast, large depth of field, minimal motion blur, and minimal reflections. However, these conditions compete for the same resources of light, resolution, capture speed, and optics, leading to a delicate balancing act.

Sourced confetti has a glossy white finish on its top surface, with exposed tan paperboard elsewhere. These colors being light, are contrasted best by a dark background. A black fabric was chosen for this purpose, with the added benefit of absorption rather than reflection of light.

When using an alternative color camera during initial experiments, the confetti was colored in red, green, and blue to be tracked more easily. When in grayscale, these colors become dark and no longer contrast the background well. It was considered to color the confetti white, with a matte finish to reduce reflections. However, the idea was abandoned due to concerns about considerable weight gain, changes in stiffness, and possibly sticky surfaces, some of which were observed with the colorful confetti.

To achieve a clear picture of confetti, the entire region of interest should be in focus with motion blur eliminated. While the plane of focus can be set in the pipe, the depth of field must be large enough to extend the focus to behind and in front of it. This way, confetti will be in focus both at the top and bottom of the pipe. It is achieved by closing the aperture, at the cost of reduced light intake. To minimize motion blur the exposure time is reduced, further limiting the amount of light reaching the camera. These are the primary reasons for the large light requirements of the experiment.

For the placement of lights, the primary objective was to provide maximum light, hence they were to be placed close to the captured region. While initially suspended above the pipe, there were issues with shadows which reduced the clarity of the footage. Instead, these were placed on the opposite of each other to light the scene equally from both sides.

The acrylic pipe is a source of optical issues originating in the reflection and refraction of light. The way the junction is joined together, acrylic piping is overlaid imperfectly with unintentional air-acrylic interfaces which partially block the view at the junction. Additionally, the acrylic captures light by total internal reflection, with the pipe acting as an optical fiber. Light primarily escapes the pipe at features as the pipe ends and other imperfections, lighting them up as seen in figure 3.3. The resulting bright spots might obstruct the vision of the confetti.

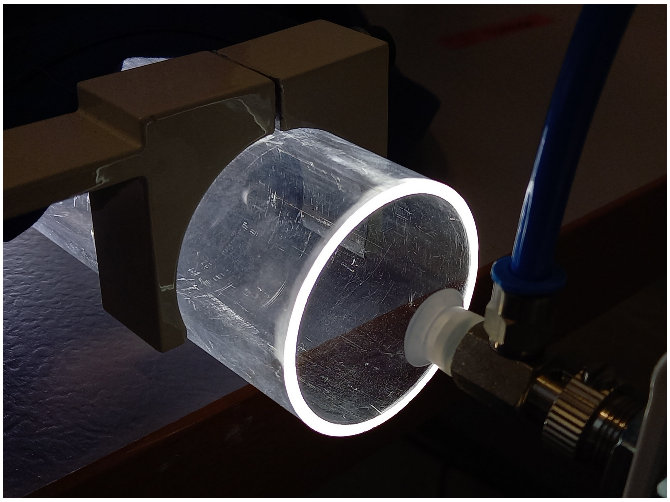

Figure 3.3: Illumination caused by totally reflected light.

Another issue from refraction and reflection is the potential of virtual objects, which might be confused for real objects. With static lights, their virtual counterpart will appear in the same locations and can be filtered out. The issue with virtual confetti is that these move and can be approximately as bright as real confetti. To tell real and virtual confetti apart was difficult with computer vision.

Since reflected light becomes partially polarized during refraction and reflection at the interface between optical mediums, polarization filters could potentially remove virtual confetti. In tests, multiple confetti were placed in the junction, while a filter was rotated in front of the camera lens. Exemplified in figure 3.4, is how the polarization filter cannot filter out all virtual confetti simultaneously.

Beginning with figure 3.4a, two prominent virtual confetti are present within the red and blue regions. For another orientation of the polarization filter, shown in figure 3.4b, the virtual confetti within the blue region is almost entirely gone. Simultaneously, the one within the red region becomes slightly brighter.

(a) Two prominent virtual confetti.

(b) One prominent virtual confetti.

Figure 3.4: Effect of polarization filter on virtual confetti in two orientations. A red and a blue region mark the position of two virtual confetti.

That all virtual confetti cannot be filtered simultaneously is likely caused by a difference in polarization direction originating from the curved surface of the pipe. Unable to efficiently filter out virtual confetti and with the cost of reduced light intake, a choice was made to abandon the use of filters.

3.3 Computer Vision

Within the previous works, confetti positions were extracted by hand for each frame of each recording. This process was tedious and limited the amount of data that could be extracted. To more efficiently extract data from more recordings, the extraction was to be aided by computer vision scripting. In this thesis, the Open Computer Vision Library (OpenCV) was used for Python.

Initially, computer vision trackers were used to follow the confetti. These operate by identifying similar features in different frames, using previous identifications as references. However, with changing confetti orientations, virtual confetti, and visual blockage, there would not be consistent features. Because of this, the trackers were largely unreliable and were hence abandoned.

An alternative approach was to identify confetti with frame-by-frame analysis of pixel brightness values between 0 and 255. A background frame without confetti was subtracted from each frame, making all static elements black (0) and all elements with change grayscale. For increased contrast, the brightness of each frame is scaled for the brightest pixel to become white (255). An example of the resulting frame is shown top right in figure 3.5.

By thresholding the brightness, less bright elements like virtual confetti and noise are partially eliminated. The resulting frame has sharper edges and is shown at the bottom right of figure 3.5. Detection of contours is used to identify continuous regions of brightness, separated from the background. These are filtered by an area threshold, to obtain the largest regions which are assumed to represent the confetti. The centers of the large regions are used to obtain the confetti center by an area-weighted average.

The left of figure 3.5 is an input frame with overlays. All contours are drawn in red, with those above the threshold in green. All center points are yellow, and the corresponding confetti center history is pink. The entire figure is used to evaluate thresholds and to identify issues.

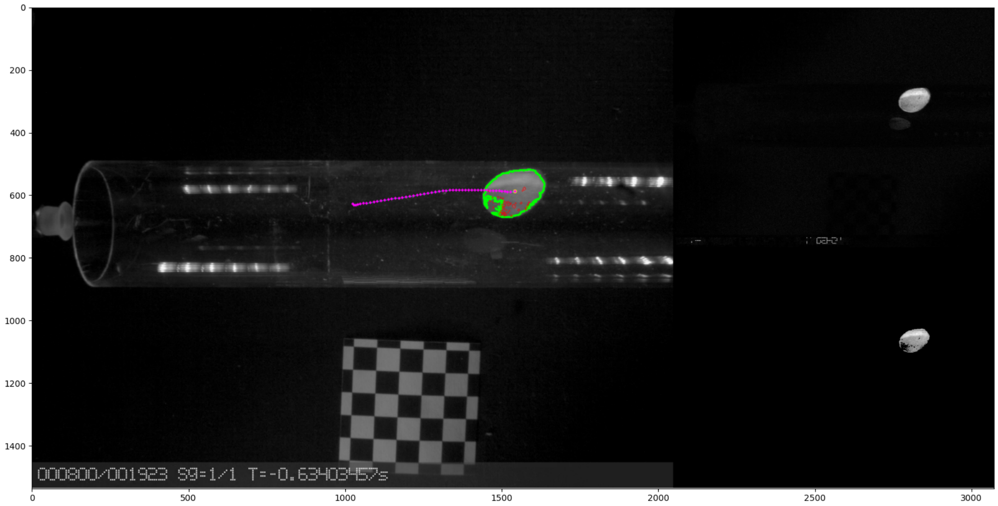

Figure 3.5: Example of frame by frame analysis.

While more reliable than the trackers, it still struggles to identify confetti confidently. For some frames, confetti is significantly harder to identify, sometimes even by eye. Examples of frames that are hard to analyze are shown in figure 3.6. Shown are cases of confetti being orthogonal to the viewing plane as a thin line, bright virtual confetti, and obstructions from the junction.

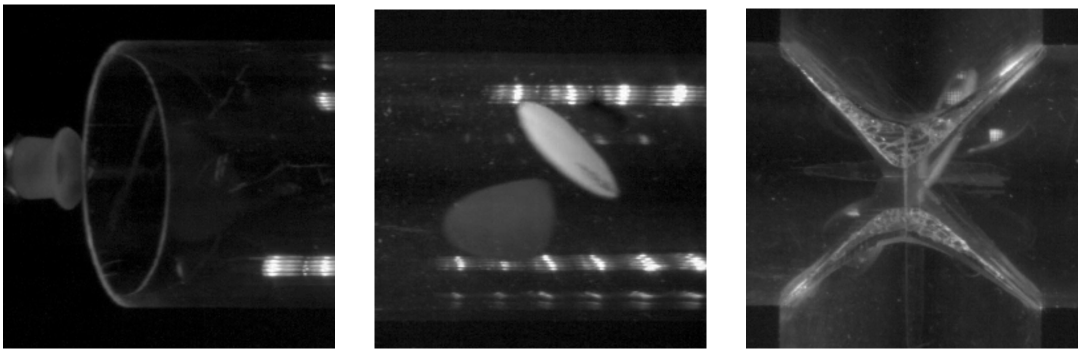

(a) Orthogonal confetti. (b) Virtual confetti. (c) Junction Obstruction.

Figure 3.6: Problematic frames for automatic extraction by frame analysis.

This unreliability makes the method unsuitable for fully automated extraction of data. Instead, these methods were utilized in an intractable script that queried the user for the selection of frames, start and end time, threshold pixel brightness, and threshold region area. Additionally, tools were added to manually mark missing data points and to allow for corrections.

The confetti positions are obtained as pixel coordinates and must be transformed into a meter-based coordinate system shared with the simulations. For this purpose, a calibration tool was created to prompt the user to mark pipe features and known distances as per figure 3.7. This defined reference points, offset rotation angles, and pixel-to-meter conversion factors, used to perform a coordinate transform. Lens distortion effects are not accounted for and might negatively impact the precision of the coordinate transfer. The final step was to save the positional and temporal data for later use.

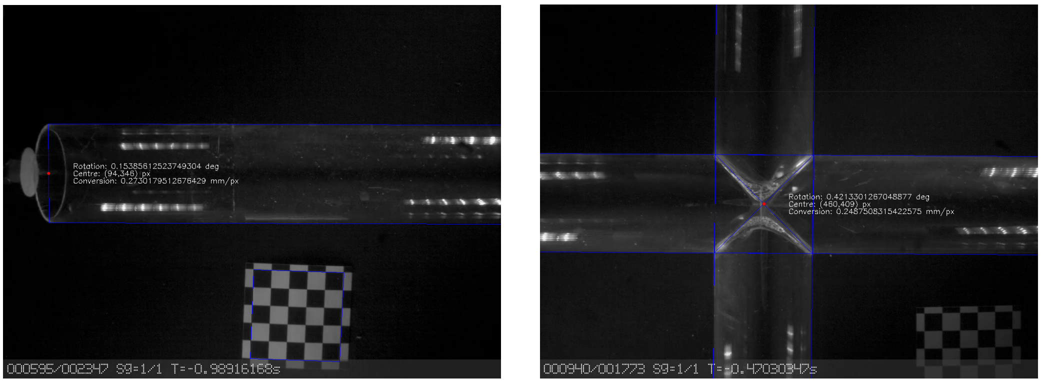

```
Rotation: 0.15385612523749304 deg
Centre: (94,346) px
Conversion: 0.2730179512676429 mm/px
000595/002347 S9=1/1 T=-0.98916168s
```

```
Rotation: 0.4213301267048877 deg
Centre: (460,409) px
Conversion: 0.2487508315422575 mm/px
000940/001773 S9=1/1 T=-0.47030347s
```

(a) Inlet calibration. (b) Junction calibration.

Figure 3.7: Examples of calibration of known features for a coordinate transform.

4 Computational Set-up

The new experimental rig will be replicated by virtual modeling. For practicality, such models are commonly constructed in commercial FEM and CFD software which all offer different methods. Models of this thesis were built within Siemens Simcenter Star-CCM+ CFD software. The development of the final model, presented here, is the culmination of more than twenty other models.

4.1 Geometry and Domain

The geometry is created from the part drawing seen in figure 3.1. In complementary measurements using a caliper, the outer and inner diameter was measured to 50 mm and 45 mm respectively. From measurements for the experiments, the confetti is idealized as flat cylinders with a diameter of 25 mm. Since the thickness could not be measured accurately, an approximate thickness of 0.35 mm is assumed. Created with built-in CAD utilities in Star, these became the base geometry for the simulation.

For modeling purposes, this geometry was modified in two ways to improve simulation quality and effectiveness. The first was to extend the computational domain around each inlet, allowing the confetti to be placed outside the pipe, as in the experiments. The second was to shorten the outlet pipe to reduce computational costs. These modifications are motivated in the results sections 5.1.2 and 5.1.3.

The final domain is visualized in figure 4.1. The fluid occupies the inside of the pipe and the inlet extensions, excluding confetti which are placed parallel and centered to the inlets, a centimeter in front of each. While three confetti are present in the figure, only simulations with one confetti will be analyzed in this thesis.

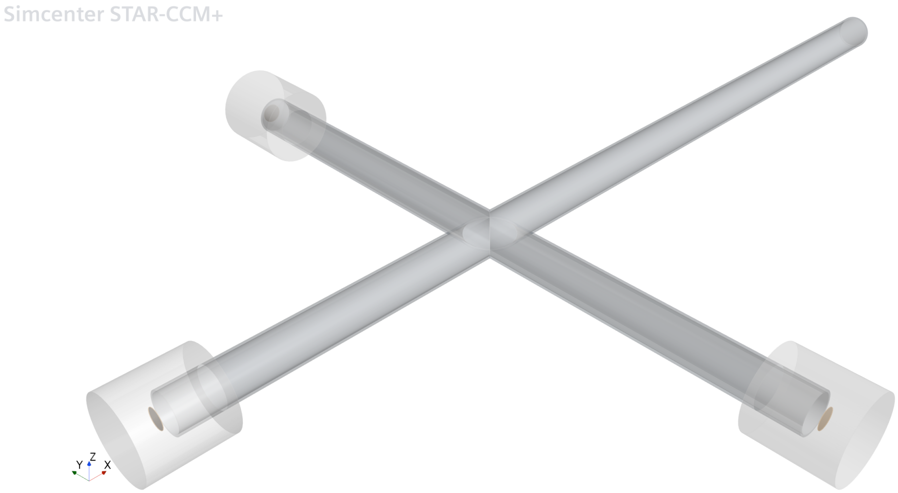

Figure 4.1: Overview of the computational domain, with inlet extensions and shortening.

4.2 Overset

An overset approach is used to accommodate the motion of the confetti. Attached to the confetti surface, its computational domain follows the confetti. Created from the confetti with an offset of 8 mm, it forms a cylinder with a height of 16.35 mm and a diameter of 41 mm. Its edges are rounded off by fillets with a radius of 1 mm. The resulting overset domain is shown in figure 4.2.

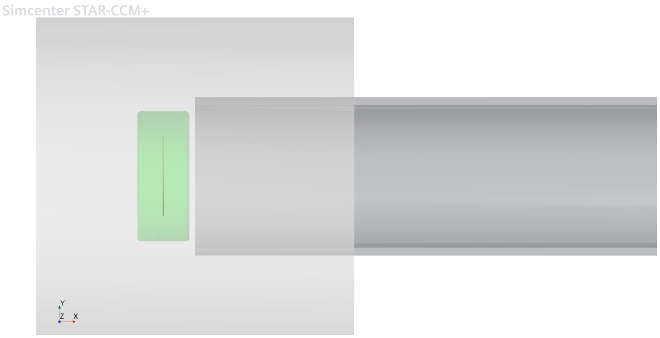

Figure 4.2: Inlet domain with the overset region in green.

The overset domain is attached to the confetti surface and is morphed when the confetti is deformed. It follows the confetti by translation and rotation. In comparison to alternative methods for motion, the overset method had the best potential for computational efficiency and was more robust compared to the other plausible approach of general re-meshing, also used in the development process.

4.3 Mesh

The solid domain representing the confetti has its top surface automatically meshed with quadrilateral elements with a base size of 2 mm. Extruding the surface mesh across its height by two layers, a total of 374 hexahedral cells represent the confetti geometry. The final confetti mesh is shown in figure 4.3.

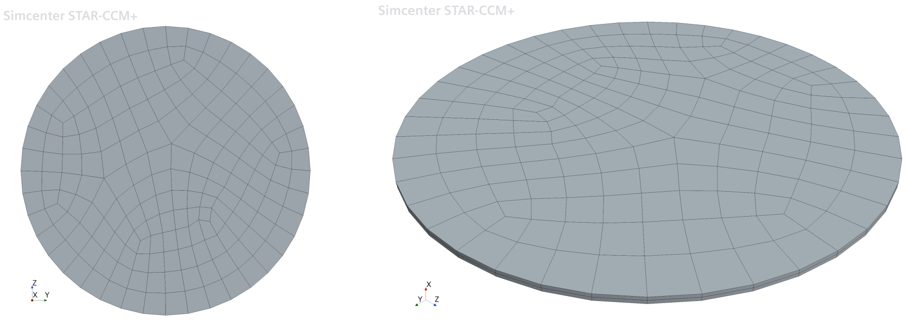

(a) Top-down view

(b) Isometric view

Figure 4.3: Solid confetti mesh.

For the contact model used by the solid solver, an enclosed tessellated surface is required. Hence, the outer pipe geometry surface is roughly meshed with triangular elements with a base size of 10 mm. Following model recommendations, the internal surface is meshed with the same base size as the confetti (2 mm). The resulting surface mesh is shown in figure 4.4 beneath.

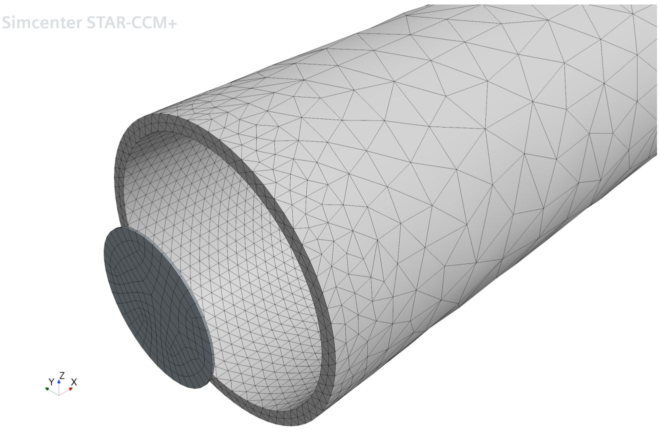

Figure 4.4: Surface contact mesh.

Discretization of both the fluid and the overlaid overset domain is done by an automated meshing procedure. Polyhedral elements are used to discretize their volumes using their base size of 1 and 0.75 mm respectively. Smaller elements are present near confetti and pipe walls, adjusted to the surface triangle mesh down to a fourth of the base size. Additionally, prism layers are used at these surfaces to properly resolve the flow near the wall. These consist of two layers with a stretch factor of 1.5 and a total thickness of 8% of their base size.

The resulting background mesh contains 30,000,000 cells and is shown in figure 4.5, accompanied by the overset mesh of 330,000 cells in figure 4.6. Both display the thin wall layer elements and the cell growth towards the center and away from the confetti.

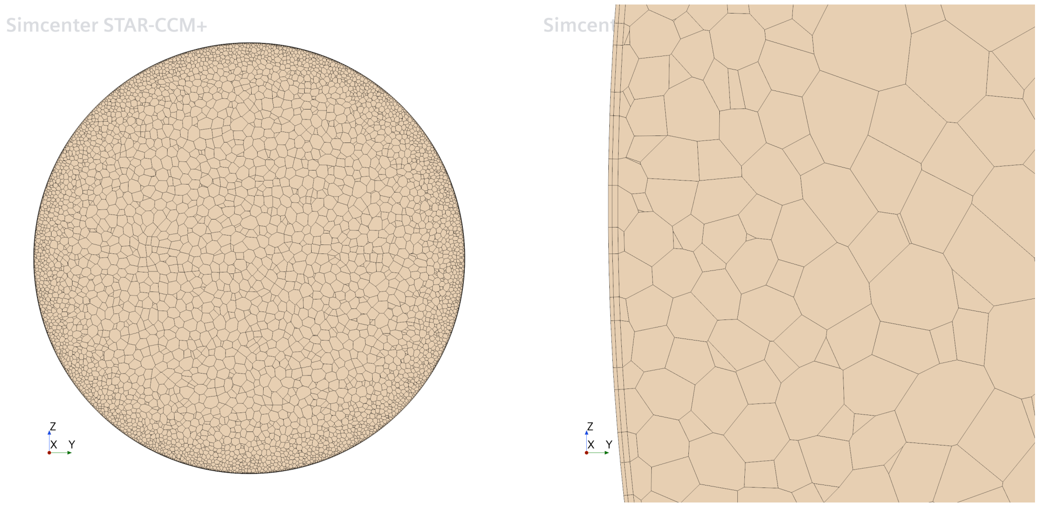

(a) Cross-section.

(b) Prism layer zoom.

Figure 4.5: Background pipe mesh.

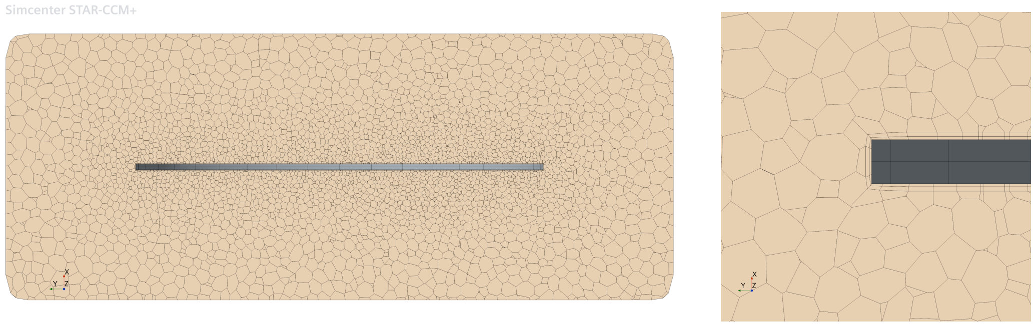

(a) Cross-section.

(b) Prism layer zoom.

Figure 4.6: Overset pipe mesh.

With changes near the thesis termination, there were no possibilities for a conventional mesh sensitivity study. Because of this, the meshing was made intentionally finer than a previous morphing-re-meshing model, which had a base size of 2 mm, which was indicated as sufficient. An in-depth study was performed in Christierson's thesis, from which the final mesh was constructed with 21,000,000 cells [3]. Considering the slightly larger domain in this thesis, the mesh should be of similar quality.

4.4 Boundary Conditions

All boundaries are illustrated with individual colors in figure 4.7. Assigned to the background domain are the inlets (green), the outlet (red), and the pipe walls (gray). The overset has confetti walls (gray) and an overset interface (blue).

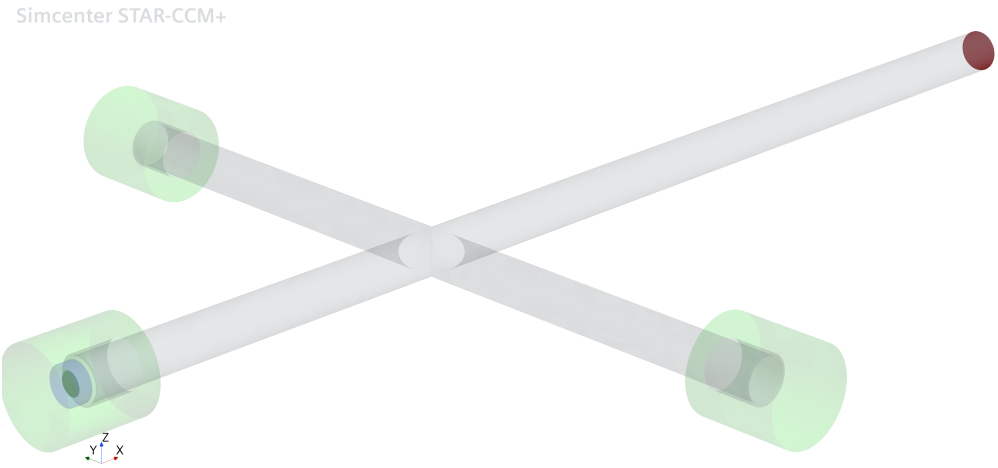

Figure 4.7: Illustrated boundary conditions. Green inlet, red outlet, outlet, gray walls, and blue overset.

The three inlets are set as stagnation inlets, where the flow enters the domain boundary-normal at zero pressure. The mass flow outlet is driving the flow by a rate of 32.6718 g/s, derived from the fixed air density 1.184 kg/m^3, anemometer diameter and corresponding speed measurement of the experimental result section 5.1.1. Walls of both pipes and confetti are assumed as no-slip walls, with zero velocity at all wall surfaces.

Contact between confetti and the pipe was enforced by a frictionless penalty method. It had two primary properties, penalty stiffness, and contact gap offset which were extensively tested in different combinations and compared against experiments. A penalty stiffness of 1e13 Pa/m was recommended and tests were done between 1e5 and 1e20 Pa/m. Based on results in section 5.1.5, 1e12 Pa/m was chosen. Concerning the contact gap offset, it was chosen as -1 mm based on the tested range of -2.5 to 0 mm. For additional robustness, the contact linearization was set as partial rather than complete.

4.5 Initial Conditions

To initialize the flow fields, the stress solver is disabled and a transient of 0.25 seconds is simulated for the fluid to converge to fully developed flow. The resulting flow field serves as the initial condition, into which the confetti is released by enabling the stress solver. One confetti is present in each simulation, and its placement is not constant.

Figure 4.8 illustrates variations in the initial confetti orientation. The default is shown in figure 4.8a, with the confetti parallel to the pipe inlet, one centimeter outside of it. Variations come in the form of rotation about the Z and X/Y axis, as per figure 4.8b and 4.8c respectively, by 10, 20, and 30 degrees.

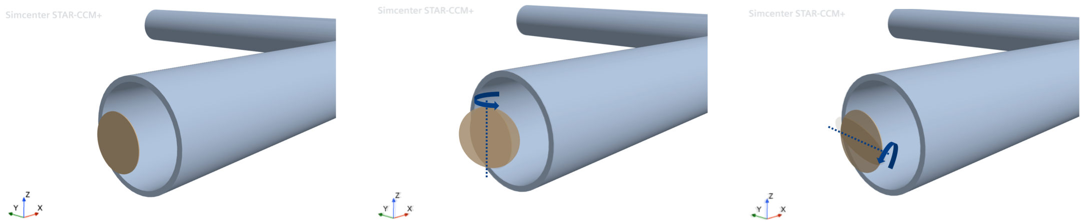

(a) Default orientation (b) Rotation about Z-axis. (c) Rotation about X/Y-axis.

Figure 4.8: Initial orientations of confetti.

4.6 Models

The paperboard confetti is modeled as an isotropic linear elastic material. With different material composites for different packages, a range of material properties were sourced. A density of 1300 kg/m^3 was thought representative alongside a Poisson's Ratio of 0.4. Differing values of Young's modulus were given in different material directions and while first interpolated to approximately 10 GPa, the modulus and later adapted to 1 GPa since confetti behavior became more similar to experiments. The confetti is also affected by a gravitational pull of -9.81 m/s^2 along the Z-axis.

The air was idealized as an incompressible gas with a constant density of 1.18415 kg/m^3 and a dynamic viscosity of 1.85508e-5 Pa-s. To model turbulence within the flow, the k-ω SST RANS turbulence model was chosen based on theoretical advantages and results compared to other models in the result section 5.1.4. It is paired with an all-y+ wall treatment model to ensure well-resolved boundary layers.

4.7 Solvers

The fluid is solved by a segregated flow solver using the implicit SIMPLEC scheme. Most of the default solver parameters were used, alongside velocity under-relaxation and algebraic multigrid methods. The solid is solved using a Newton-Raphson stepping method with a single load step, with a maximum of 20 Newton steps. Second-order temporal discretization is used with an implicit solver. Time steps are adaptive, based on a target maximum displacement of 0.5 mm of the solid confetti domain. The initial time step is set as 5 ms, used during initialization, with a minimum of 0.5 ms.

Simulations are terminated when the confetti is outside the experimental regions of interest, when its center passes 0.25 m along the X-axis, to reduce the computational cost. All simulations were performed with four academic licenses on Tetra Pak's compute cluster, each using five 32-core compute nodes for a total of 160 cores.

5 Results and Discussion

This chapter provides a comprehensive presentation of findings, paired with an analyzing discussion. It is opened with key results from the development which led to decisions in the final methodology. Results came from a total of 100 experiments and 20 simulations, analyzed separately and then compared with each other.

5.1 Results from Developmental Studies

5.1.1 Flow Measurements

The anemometer flow measurements were performed for five minutes. Recording the displays of the extraction system and anemometer, speeds were read for each second. Plotting the separate speeds against each other as per figure 5.1, it is revealed that large variations observed on the extraction system are not reflected in speeds measured with the anemometer.

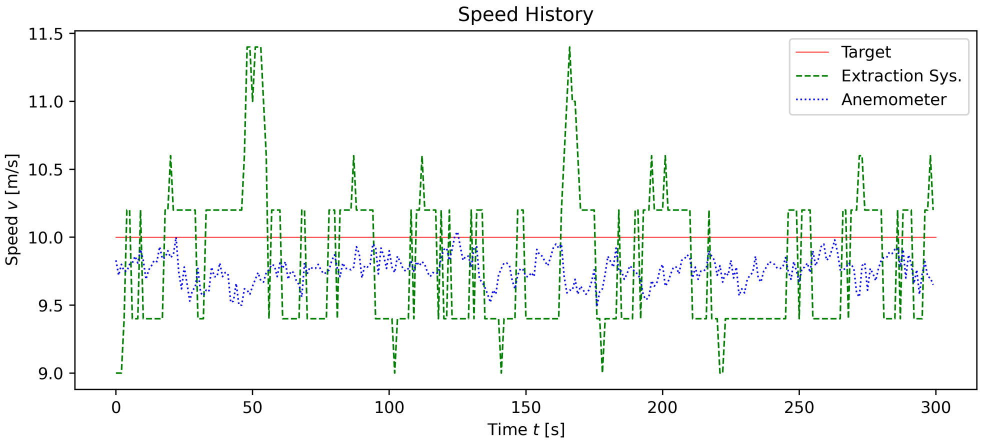

Figure 5.1: Speed measurements of anemometer and vacuum during 300 seconds.

Considering the anemometer is designed for this application and is professionally calibrated, it was argued that its measurements are more reliable than the extraction system. For the anemometer, the measured speed is plotted with the specified accuracy of $\pm|0.015v + 0.1|$ m/s in figure 5.2.

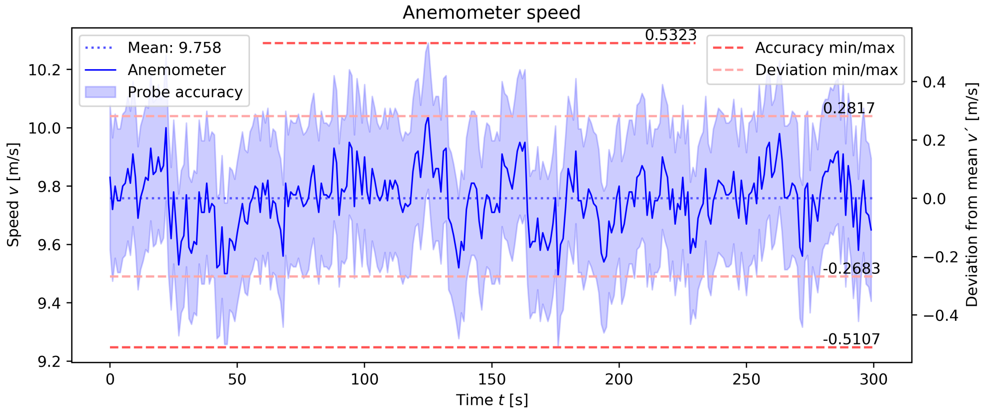

Figure 5.2: Anemometer speed plotted with its accuracy specifications and maximum deviations from its mean.

Additionally, the maximum deviation from the mean is plotted with and without accuracy. The mean is calculated to be 9.758 m/s, from which measurements deviate by a maximum of 0.2817 m/s or 2.9 % from the mean. With measurement accuracy, the deviation is a maximum of 0.5323 m/s or 5.5 % from the mean.

5.1.2 Inlet Extension

The inlet extension was designed through an iterative process to obtain a more accurate description of the experiment conditions. In addition to correct confetti placement outside the pipes, some models from the development process had velocity inlet boundaries with velocities obtained from uncertain anemometer measurements. With the extension present, the boundary conditions could be replaced with mass flow outlets, with a more precisely measured outlet mass flow. This change led to entirely different velocity and pressure contours, seen in figure 5.3, thought to be more accurate.

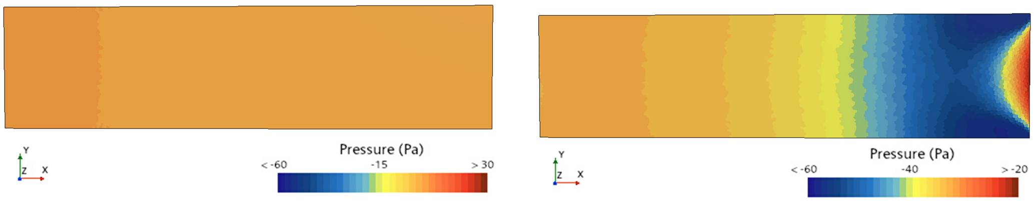

(a) Pressure without extension.

(b) Pressure with extension.

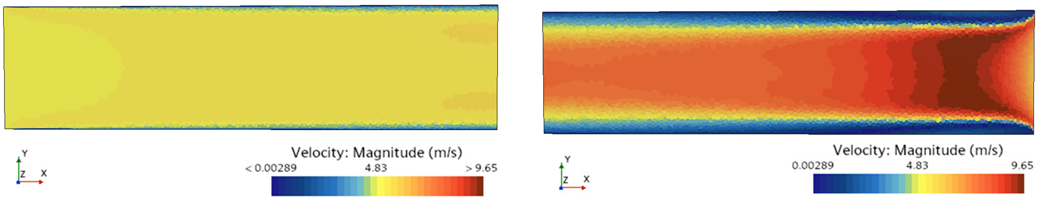

(c) Velocity without extension.

(d) Velocity with extension.

Figure 5.3: Velocity and pressure contours at the inlet, with and without an inlet extension.

These contours were produced without pipe wall thickness using baffles. With this configuration, there was significant detachment of flow from the pipe edges as seen in figure 5.3d. Intuitively it seemed unreasonable, hence the wall thickness was added for all models to be more true to experiments.

Different shapes and sizes were tested to optimize the inlet extension geometry. From the sensitivity analysis, it was decided that a cylindrical extension would have minimal cost and accommodate boundary conditions the best. The cylinder was centered around the pipe inlet with a radius of 0.05 m and a height of 0.1 m.

For verification that inlet flow conditions were not significantly affected by the nearby boundaries, two steady-state solutions were computed. One for the decided dimensions and one for much larger ones with a radius and height of 0.2 m and 0.4 m. Corresponding velocity contours are shown in figure 5.4.

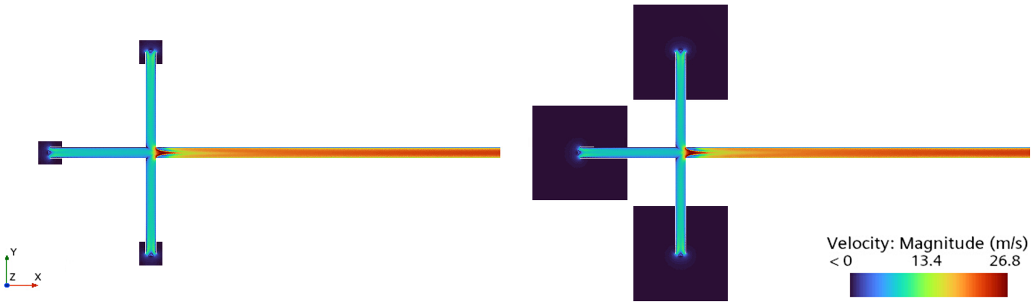

(a) Full domain view.

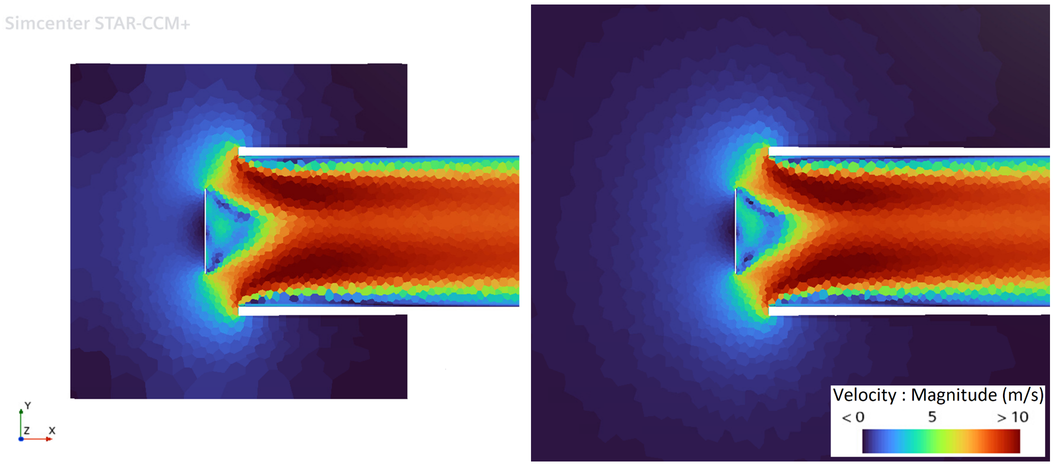

(b) Inlet focused view.

Figure 5.4: Velocity contours for chosen shape (left) and largest possible shape (right).

While the results are seemingly identical on the contour plots, differences are better quantified by velocity profiles. From the confetti 10 mm outside the pipe to 10 mm inside it, profiles on probe lines were spaced by 5 mm and resulted in figure 5.5. The profiles are similar, with differences attributed to their slightly different meshes, motivating that the chosen dimensions are reasonable.

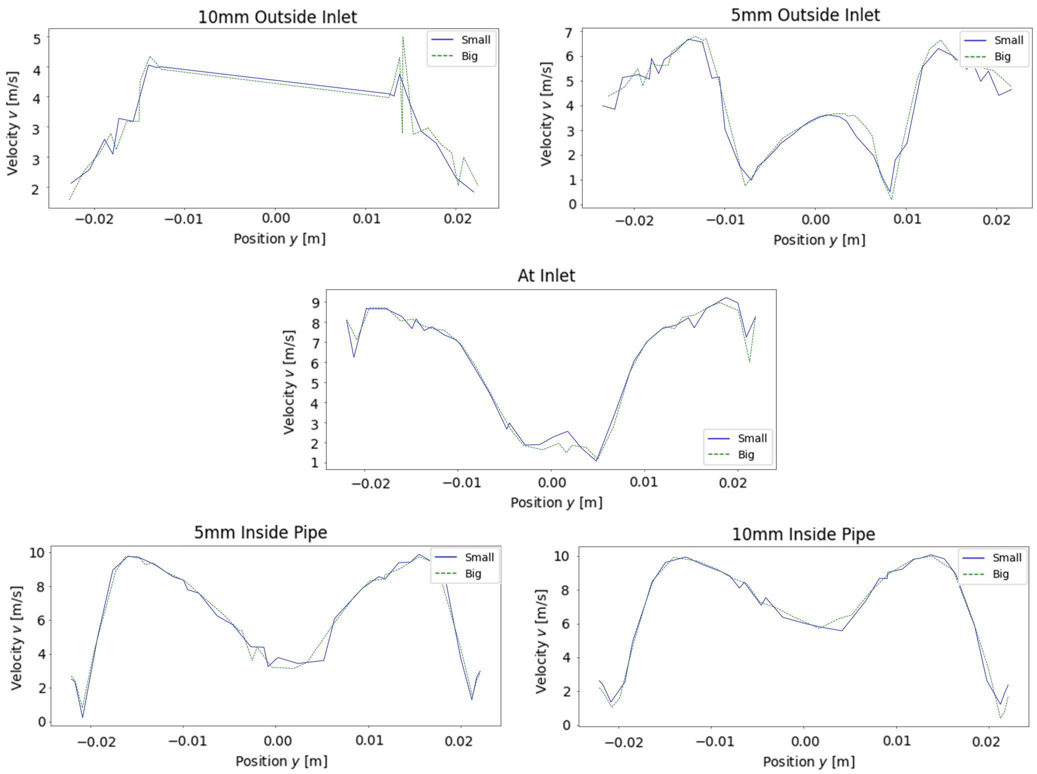

Figure 5.5: Velocity profiles on probe lines near the inlet, spaced by 5 mm, for chosen shape (blue) and largest possible shape (green) of the inlet extension.

5.1.3 Pipe shortening

During the majority of development, a general re-meshing methodology was used for motion. It demanded efficient meshing procedures, much more than the final model using an overset mesh. With the confetti not being recorded more than 0.25 m downstream of the junction, the outlet pipe was shortened by 0.625 m (40 %) to reduce domain size and consequently the computational cost.

Again computing two steady-state solutions, with and without shortening of the domain, velocity profiles on probe lines within the pipe were extracted. Presented in figure 5.6, these show that the velocity profiles differ near the outlet, 0.8 m downstream of the junction. Differences begin to show at 0.5 m, but as simulations stopped when confetti passed 0.25 m, the shortening should not affect the results negatively. While slight differences are also observed near the junction, these are thought to originate in small differences between the two meshes.

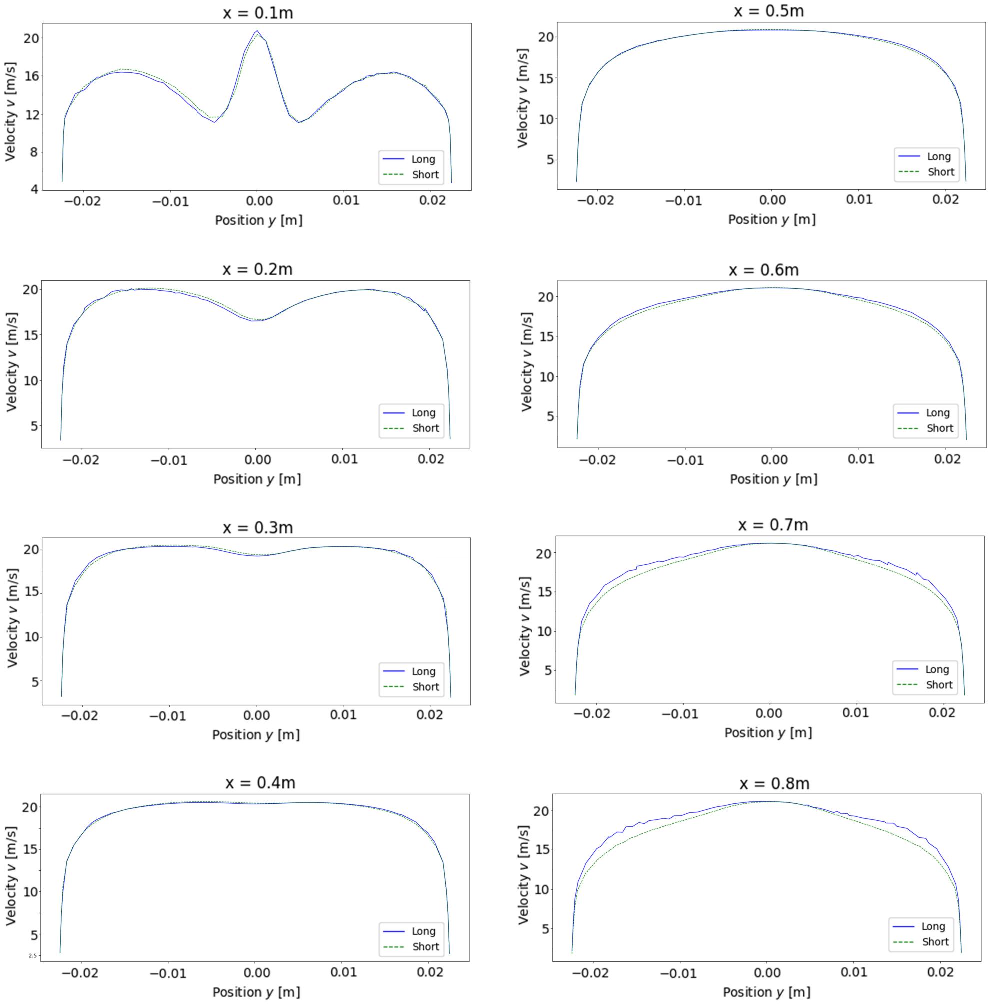

Figure 5.6: Velocity profiles in the pipe from equally spaced probes for the full and the shortened domain.

5.1.4 Turbulence model

While the k-ω SST model was indicated as the best choice by theory, its performance was tested against both the k-ε Realizable model and Reynold Stress Model RSM. Steady-state simulations were performed before geometry optimization of inlet extensions and pipe shortening, using a fine hexahedral mesh which ensured low-y^+ wall treatment by keeping all y^+ values beneath five.

Velocity contours are presented in figure 5.7 by two alternative cutting planes. While RSM is assumed the most complete description, it is more expensive than the other two and does not guarantee more correct results. Assumed too expensive for this application, it is used as a reference in the absence of an experimental reference. However, neither k-ω nor k-ε produces equivalent results.

Focusing on the junction, the velocities seem best replicated by the k-ω model and would be preferred. However, it does under-predict the size of recirculation regions compared to the two other models and the flow is not as uniform downstream as for RSM. It is still chosen, mostly because it is supported by theory for internal flows over k-ε.

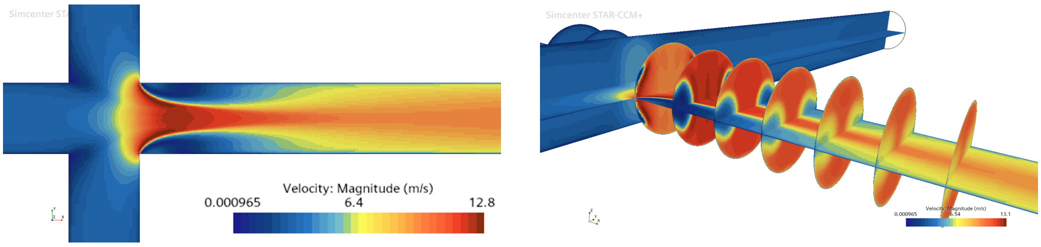

(a) k-ε Realizable (b) k-ε Realizable

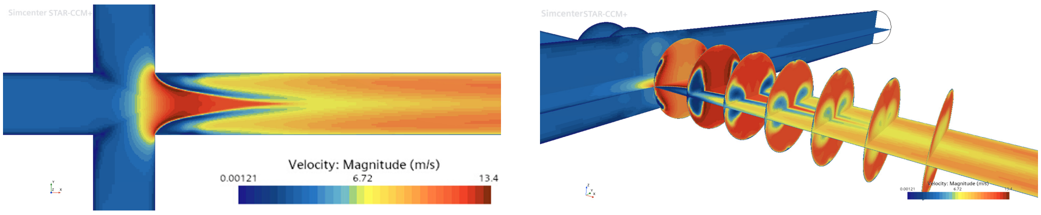

(c) k-ω SST (d) k-ω SST

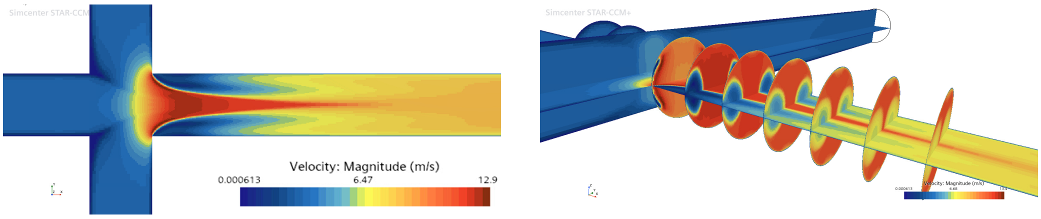

(e) RSM (f) RSM

Figure 5.7: Velocity contours for a selection of common RANS turbulence models.

5.1.5 Contact model

For validation of the contact model, confetti was recorded when dropped from the top of the pipe. Used as a reference for simulated drops, they showed that confetti rarely bounced more than twice and never to a height greater than a couple of millimeters. A typical series of events is shown in figure 5.8.

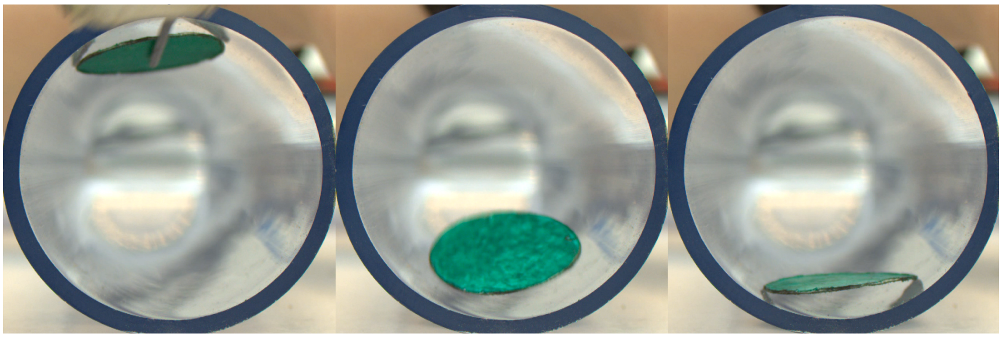

Figure 5.8: Experiment of confetti being dropped within the pipe. Initial position (left), rebound height (center), and rest(right).

To tune the contact model in simulations, the two primary properties of penalty stiffness and contact gap offset were tested in more than 30 combinations, observing trends in confetti behavior. In general, a decreased penalty stiffness led to less violent impacts but if chosen too small it could not reflect the confetti before it penetrated the pipe, crashing the simulation. To counter this, a larger contact gap offset led to increased robustness as confetti had more distance to be reflected at the cost of possible unphysical reflections away from the actual wall.

Decreasing the original penalty stiffness to 1e12 Pa/m coupled with a 1 mm contact gap offset, gave less energetic contacts. A simulation using these properties is illustrated by snapshots in figure 5.9, not too dissimilar to what was observed in figure 5.8. While a smaller offset of 0.25 mm could be used in this model, it was not robust enough to be used in the final model, because of the high velocities experienced by the confetti during their transport toward the exhaust pipe.

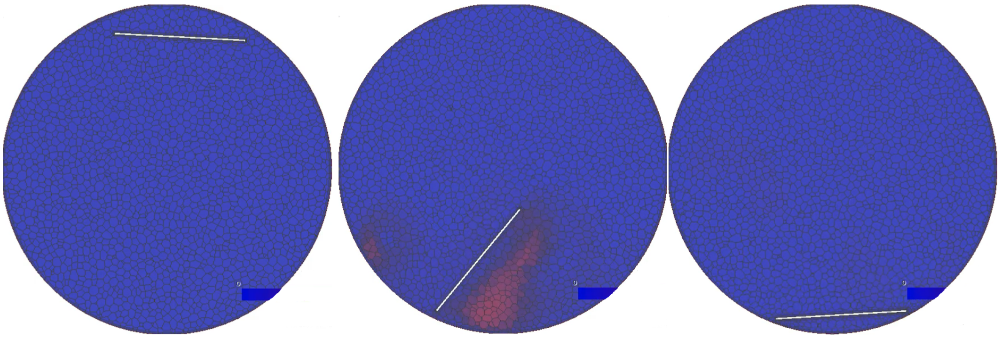

Figure 5.9: Simulation of confetti being dropped within the pipe. Initial position (left), rebound height (center), and rest(right).

5.2 Experiments

The experiments consisted of 100 releases of confetti, divided into four batches of 25. Half were released from the top inlet, dubbed *confetti 1*, and assigned a blue color, with their counterpart released from the left inlet colored in red and dubbed *confetti 2*. Half of each 50 releases were recorded overlooking the corresponding inlet, with the others overlooking the junction.

A total of 18 049 data points containing coordinates and time relative to the first entry, were extracted from the recordings. Although most points were extracted automatically, all recordings were corrected by manual marking, affecting upwards of 20% of all points, due to the complications shown in figure 3.6.

While time is accurately extracted from the recording info bar, positions are prone to user error from manual marking and imperfect extraction scripting. Consistent pixel-perfect markings for confetti centers are unlikely, and each pixel represents roughly 0.25 mm. Furthermore, the camera lens introduces slight distortion near the frame edges which leads to an unquantified error for the coordinates.

5.2.1 Static charges

When fetching confetti from the extraction system, it was noted that it sometimes stuck to its metallic surfaces. Assuming electrostatic attraction as the cause, it was investigated if confetti was attracted to the acrylic glass piping. Confetti might slide along its walls, resulting in an attractive charge.

To test if electrostatic attraction was possible between confetti and the junction, confetti was rubbed against the junction and dropped beside it. Some confetti was observed to deviate from a vertical path towards the junction, and few even stuck to the side of it. By figure 5.10, the confetti is shown when dropped offset the pipe and when at rest on the side of the pipe.

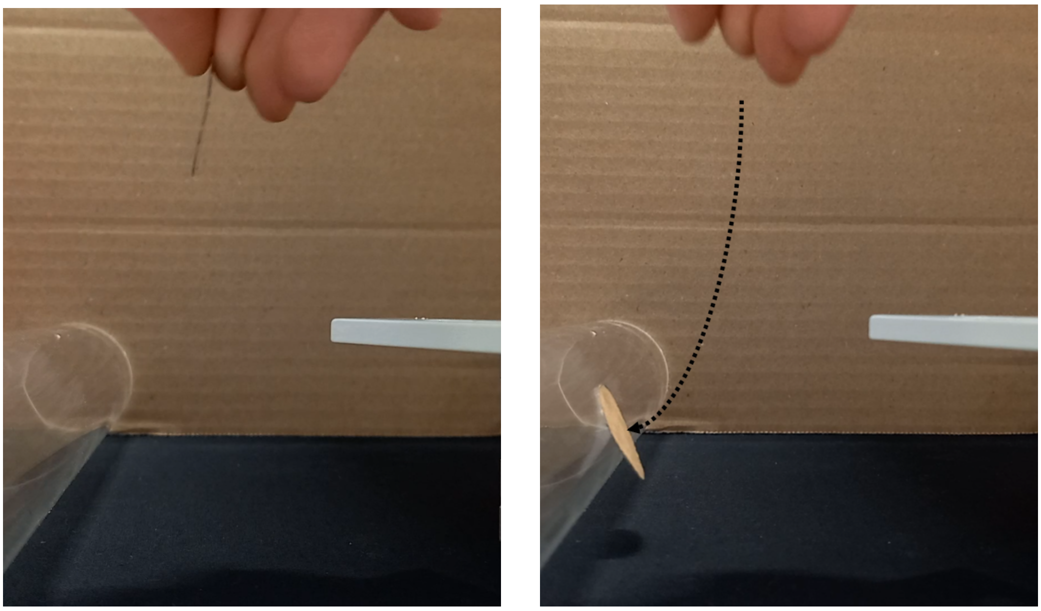

(a) Confetti when dropped.

(b) Confetti at rest, after curved trajectory.

Figure 5.10: Demonstration of static attraction between confetti and pipe.

While confirming that electrostatic attraction between the pipe and confetti is possible, it could not confirm that it is present or quantify its possible impact. While further investigation is needed, it might be a contributing factor alongside friction for confetti getting stuck as per the issues presented in figure 1.2a and b.

5.2.2 Trajectories

All experiment trajectories are plotted together in figure 5.11 alongside pipe boundaries in the symmetry plane and six regions of interest (ROI). From this overview, confetti 1 is observed distributed with a bias towards one side of the inlet pipe while within region 1. Sometimes it exhibits the negative trait entering the opposite inlet. Confetti 2 traverses the pipe along the X-axis, seemingly unbiased to any wall in region 3.

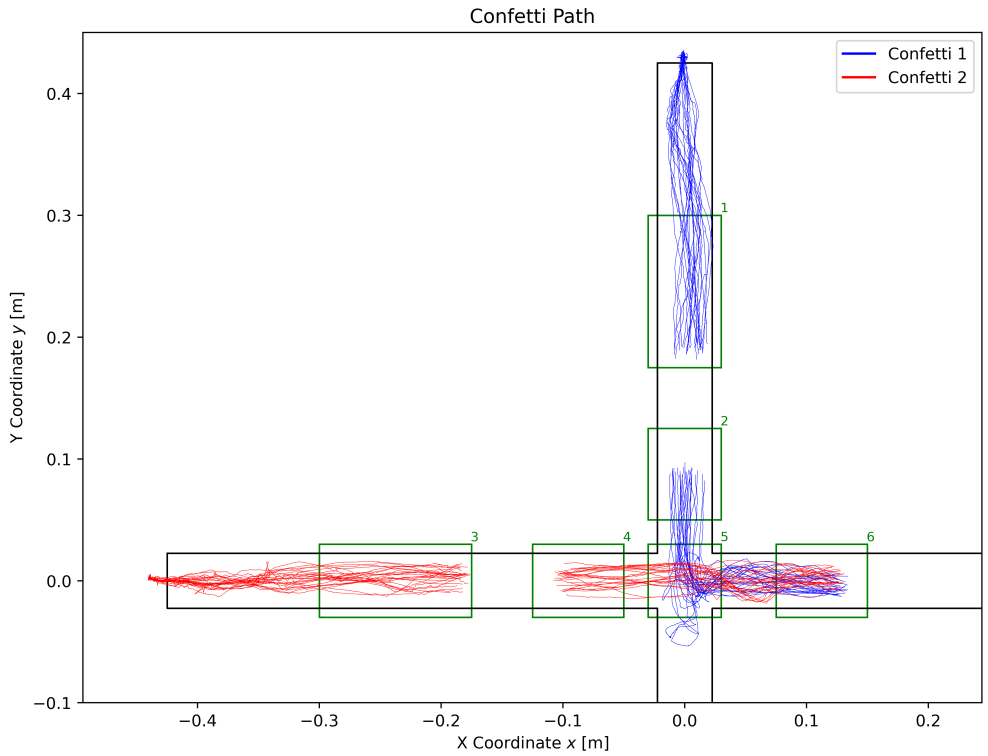

Figure 5.11: Experimental paths from a hundred experiments, in batches of 25 confetti each. With numbered regions of interest used for analysis.

For a more thorough analysis of the trajectories, each batch is framed with each trajectory plotted with different colors. Beginning with figure 5.12a, the trajectories seem to be evenly distributed initially, while biased towards positive X coordinates further downstream. One confetti is even indicated to penetrate the wall, an impossible feat.

Looking at its counterpart in 5.12b, its trajectories are evenly distributed at first seemingly biased towards positive Y coordinates around x=-0.25 m. Even further downstream, the paths are relatively centered. This might be due to the confetti being forced down in height by gravity, where the pipe is less wide.

Both batches show a combination of relatively straight paths, and winding paths spanning the pipe width. Positions near the release point are scattered, a result of uncertain markings due to blockage.

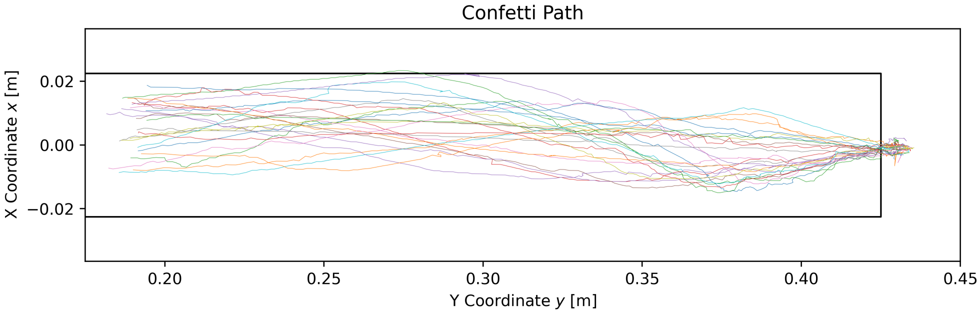

(a) Confetti 1 (top)

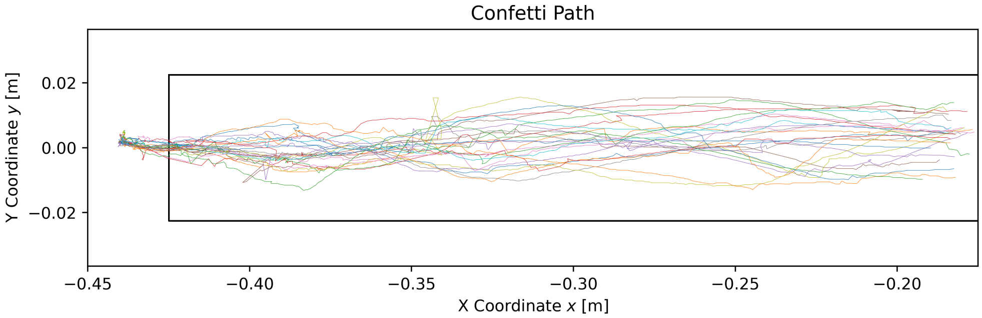

(b) Confetti 2 (side)

Figure 5.12: Experimental paths at the inlet, 25 from each confetti.

Switching to batches recorded at the junction, the trajectories shown in 5.13 seem evenly distributed towards the center. Observing confetti 1 in figure 5.13a, three confetti enter the opposite pipe while some recirculate within the junction, before exiting into the outlet pipe. Downstream, these are slightly biased towards negative Y coordinates.

In the trajectories for confetti 2 in figure 5.13a, a band of similar straight trajectories enters the junction from the positive Y coordinates, all being deflected in the opposite direction when entering the outlet pipe. No confetti enters the other inlet pipes, all entering the outlet without recirculating in the junction. These both enter and leave the region centered to the pipe diameter.

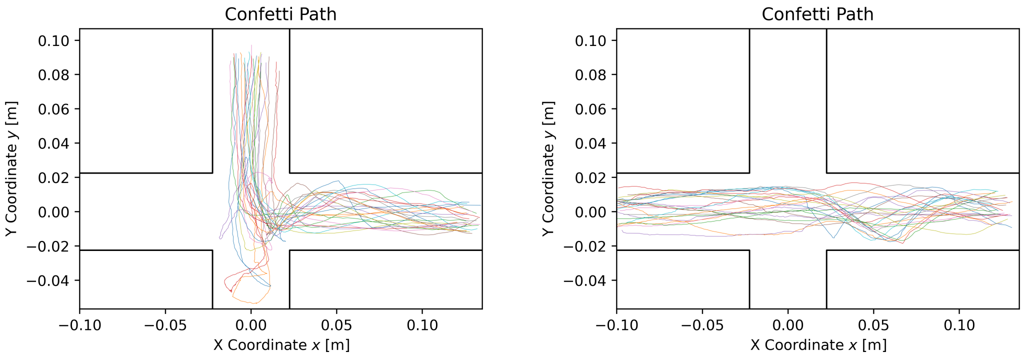

(a) Confetti 1 (top)

(b) Confetti 2 (side)

Figure 5.13: Experimental paths in junction, 25 from each confetti.

5.2.3 Positions

All coordinates are accompanied by time, but plotting against it is problematic as experiments do not share the timeline. For experiments at the inlet, zero time should be set to the release of confetti. As release is not instantaneous, the point of release cannot be determined accurately and each experiment receives different temporal frames of reference. For experiments at the junction, there is no shared reference time since the release is not captured by the camera.

With this issue in mind, the coordinate along the primary travel direction was plotted against time for confetti released at the inlet. In the figure 5.14, the slope is indicative of the velocity with steeper curves related to higher velocities. A larger spread in lines suggests more variation in velocities or bigger inaccuracies in data.

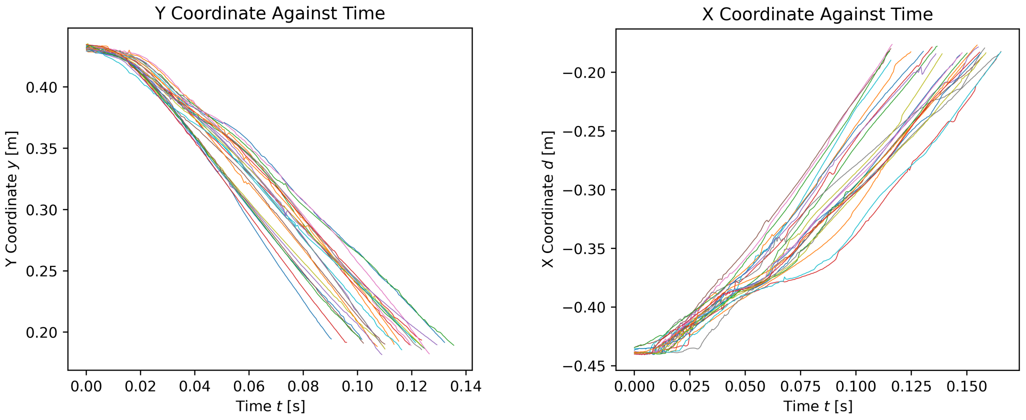

(a) Confetti 1 (top)

(b) Confetti 2 (side)

Figure 5.14: Position in the main axis of travel over time, 25 for each inlet.

From figure 5.14a, is shown to have relatively similar slopes with no features that stand out. The same could not be said for figure 5.14b, which has a larger spread and less straight lines.

To make better comparisons between the two confetti, a new but similar metric is studied. The distance between each consecutive point is calculated and compiled into the total traveled distance over time. This allows both to be plotted against each other and accounts for movement in two dimensions. Judging by figure 5.15, it is confirmed that confetti 2 has a larger spread and likely smaller speeds than confetti 1.

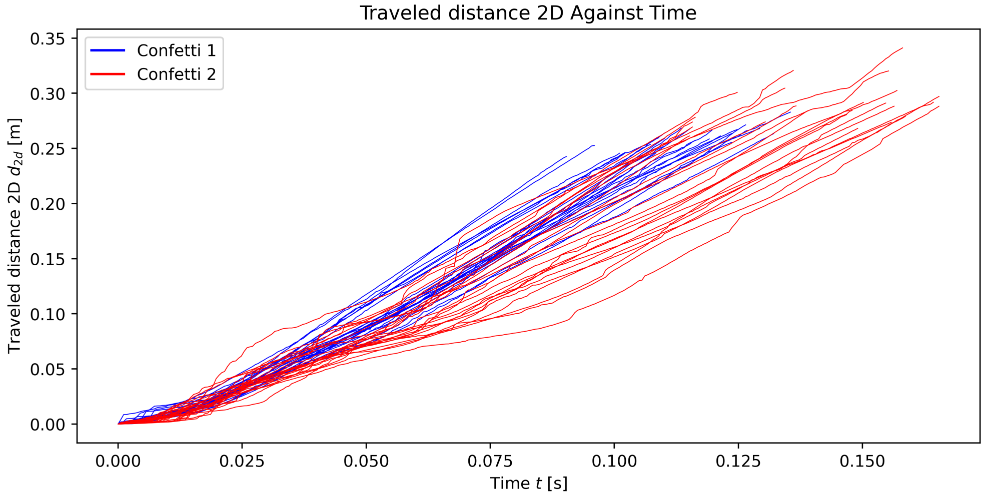

Figure 5.15: Total traveled distance (2D) against time for all experiments at the inlet.

5.2.4 Velocities

Velocity components are approximated by finite difference of coordinates against time and used to obtain the velocity magnitude. In figure 5.16, the magnitude is plotted against time for the first experiment batch for both inlets and junction recordings.

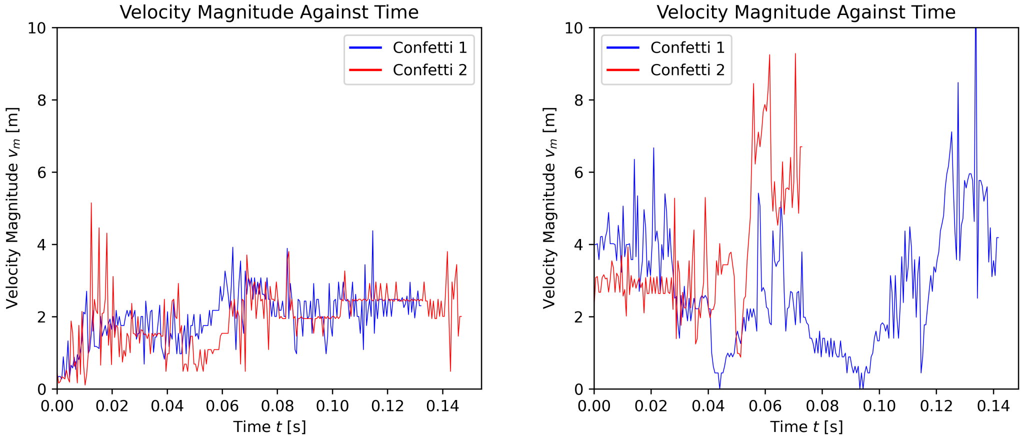

(a) Experiment at inlet.

(b) Experiment at junction.

Figure 5.16: Velocity magnitude over time for four sampled experiments. Two of each confetti, one at its inlet and one in the junction.

For a full understanding of these velocity transients, they are paired with plots of velocity magnitudes overlaid on trajectories. Beginning with figure 5.16a, it is paired with figure 5.17 which illustrates the initial gradual increase and abnormal fluctuations related to inaccurate markings, indicated by the gap after each. Also observed is a decrease in velocity at each turn near the walls, indicating contact.

For figure 5.16a, the significantly longer series and dips to zero of confetti 1, is explained by its recirculating trajectory in figure 5.18. The same figures show how the velocity increases in the outlet pipe, with temporary decreases in velocity after contact with walls.

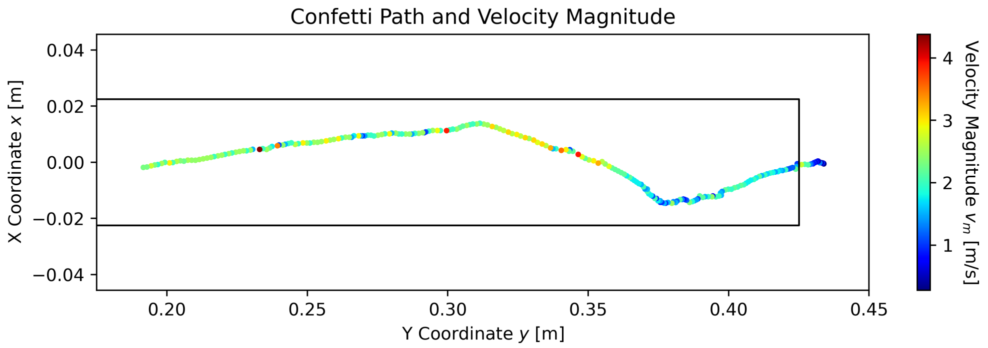

(a) Confetti 1 (top)

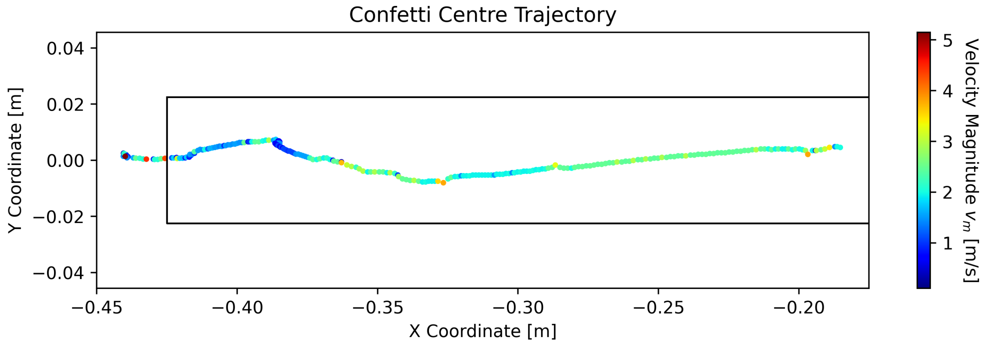

(b) Confetti 2 (side)

Figure 5.17: Velocity magnitude over trajectory. One sample experiment for each confetti at the inlet.

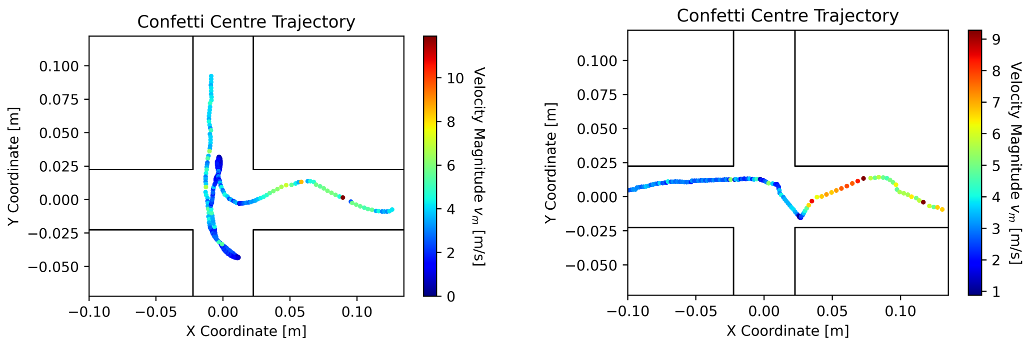

(a) Confetti 1 (top)

(b) Confetti 2 (side)

Figure 5.18: Velocity magnitude over trajectory. One sample experiment for each confetti at the junction.

While good for analysis of individual experiments, these are not useful for studying trends amongst them. For that purpose, averages of velocity magnitudes are calculated within the six regions of interest defined in figure 5.11 for each experiment, then averaged across each region.

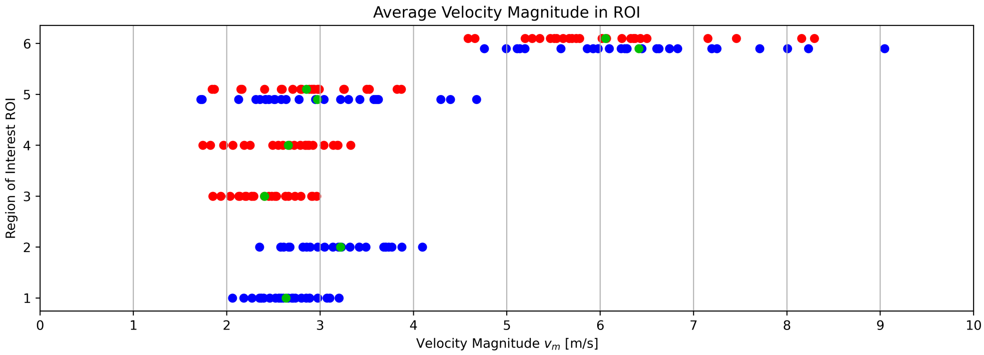

Figure 5.19: Velocity magnitude averages for experiments of confetti 1/2(blue/red) with overall region average (green).

Beginning with the region pair 1 and 3 from the middle of inlet pipes, these show similar distributions with confetti 1 having a slightly larger region average. Both have the smallest spread, not surprising since the regions contain the most data points, allowing for better suppression of abnormal velocities.

The downstream pair 2 and 4 before the junction, both have increased spreads and larger region average velocities, with a larger increase for confetti 1. This indicates that confetti continuously gains velocity until reaching the junction.

When in the junction in region 5, the spread is significantly increased for confetti 1 with a lower region average. This is not surprising since some confetti recirculates in the junction, before advancing into the outlet in region 6 with a significant gain in region average speed, and further increase in spread.

Comparatively, the confetti 2 region average is increased in region 5, and even more in region 6. Simultaneously, the spread is increased. All region averages are shown to be lower for confetti 1, compared to confetti 2. However, their spreads are often mostly shared and always increase with each step further downstream.

5.3 Simulations

The simulations consisted of a total of 20 simulations, 10 for each confetti which are dubbed and colored by the same convention as the experiments. Of each 10 simulations, 4 were made with the original position for investigation of numerical inconsistencies. The latter 6, had the confetti rotated by 10, 20, and 30 degrees around the confetti X and Y axis.

5.3.1 Consistency

In the development of predecessor models, it was discovered that identical models did not always produce the same results. Initially, two identical simulations were performed using regular single precision on identical hardware. When these produced different results the simulations were performed again, using double precision on the same hardware. Presenting all trajectories together in figure 5.20 for confetti 1 and 2, it can be seen that all four trajectories eventually differ.

Looking more closely at figure 5.20 confetti 1 trajectories of both single and double-precision simulations, are separated and become unique when within the junction. Comparably for confetti 2 in figure 5.20b, the single-precision trajectories split before the junction. While the double precision trajectories are more consistent, keeping together through the junction, they still split further downstream.

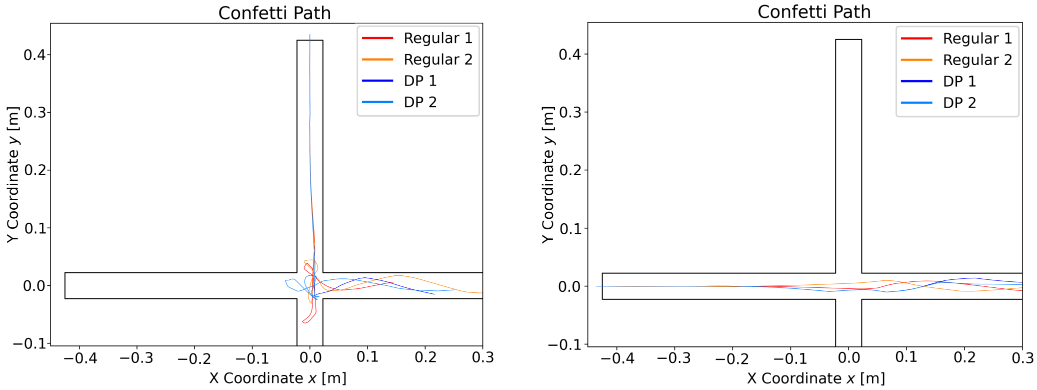

(a) Confetti 1 (top)

(b) Confetti 2 (side)

Figure 5.20: Trajectories for four identical simulations for each confetti.

In the investigation of the cause, the now available Z coordinates, plotted over time in figure 5.21, proved useful. For confetti 1, it is observed that all four simulations show the same coordinate up until the first minimum is reached, from which the two single-precision results start to differ. Similarly, differences for confetti 2 occur after minimums are reached, if the one simulation which starts differing directly is disregarded.

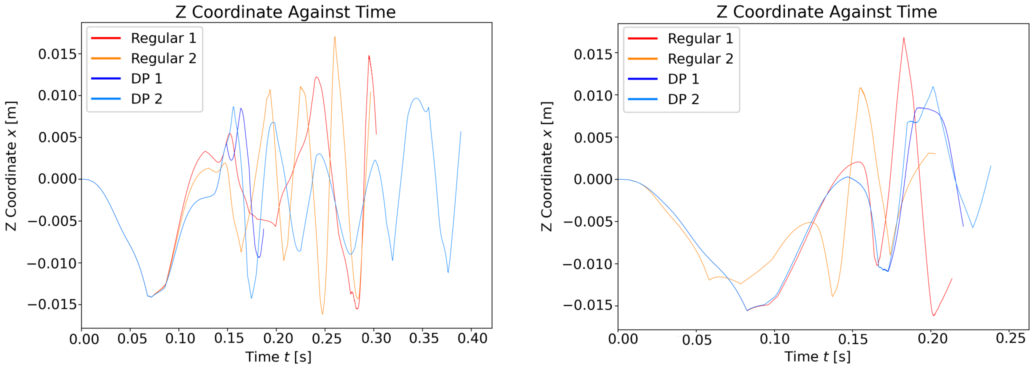

(a) Confetti 1 (top)

(b) Confetti 2 (side)

Figure 5.21: Z Coordinate against time for four identical simulations for each confetti.

As differences seem initiated at the sharp turns at minimums, the contact is suspected to initiate the differences. By taking the minimum of the contact gap field variable, the distance separating the confetti from contact is obtained. A value of zero is equivalent to contact.

When plotted against time as per figure 5.22, it is confirmed that all differences in results apart from one, are initiated from a point of contact. How it introduces randomness or errors into the simulation could not be determined, making it hard to counter. Efforts were made by lowering the time step and by increasing load steps, but these were unsuccessful. As double precision was indicated to prolong similar trajectories, it was used for all other cases.

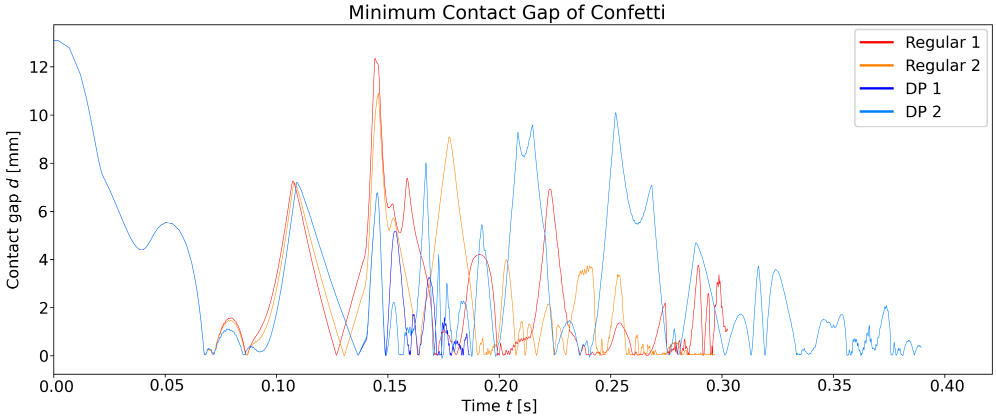

(a) Confetti 1 (top)

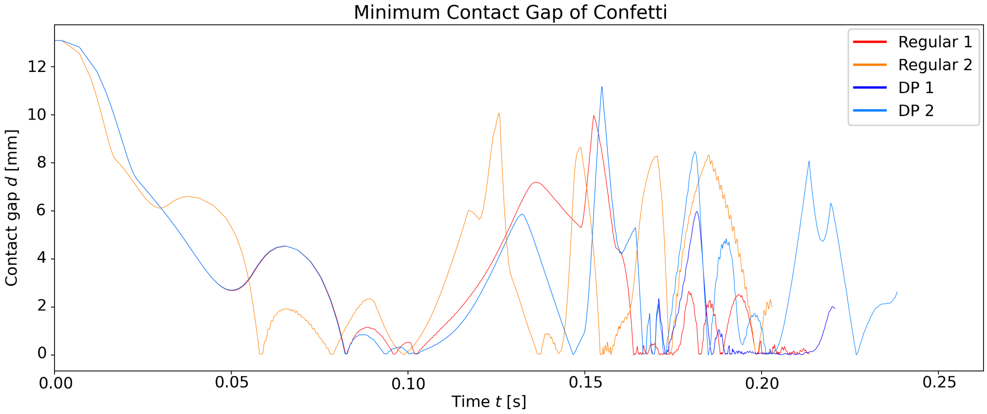

(b) Confetti 2 (side)

Figure 5.22: Contact gap minimum against time for four identical simulations for each confetti.

5.3.2 Trajectories

All simulated trajectories are presented in figure 5.23 alongside the same pipe contours and region of interest. Some confetti 1 is observed to enter both other inlet pipes, also recirculating in the junction before passing to the outlet, similar to experiments. Confetti 2 all pass directly through the junction without recirculation. Seemingly biased trajectories are thought related to simulations with an initial offset rotation.

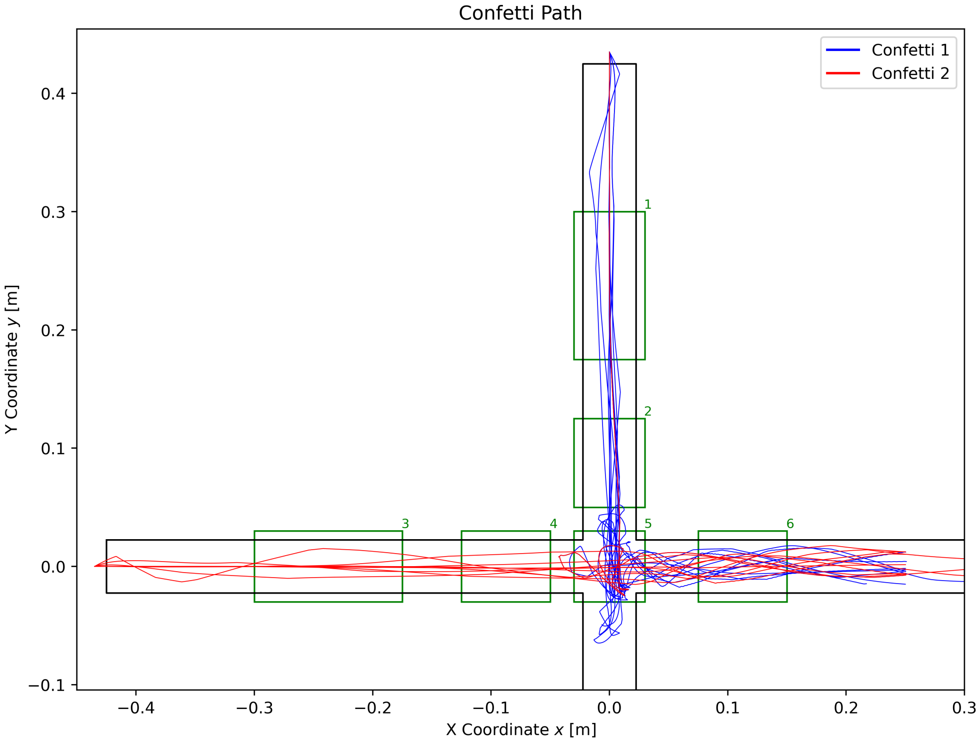

Figure 5.23: Simulated trajectories from 20 cases.

To evaluate if initial rotation is the cause of spread trajectories, they are split by rotation and presented in figures 5.24 and 5.25. When rotated around the Z axis, as per figure 4.8b, both confetti are observed to quickly deviate from the centered path of the confetti not rotated. The initial deviation for both is ordered by the magnitude of the offset rotation, which quickly shifts into a winding path.

The same behavior is not observed for rotation about the X/Y axis, as per figure 4.8c, in which confetti follows the same centered path initially. Halfway down the inlet pipe, it starts to differ, possibly initiated by wall contact.

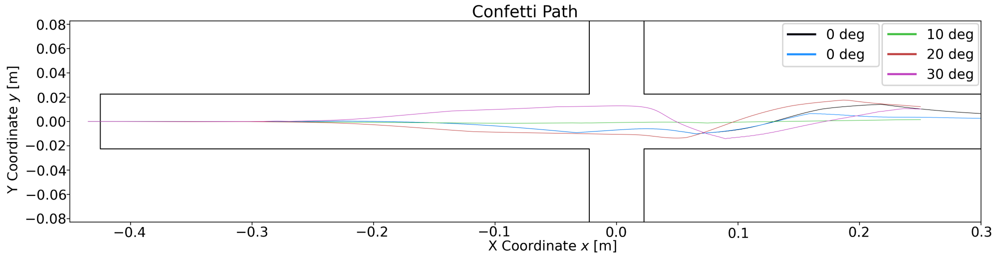

(a) Rotation around Z axis

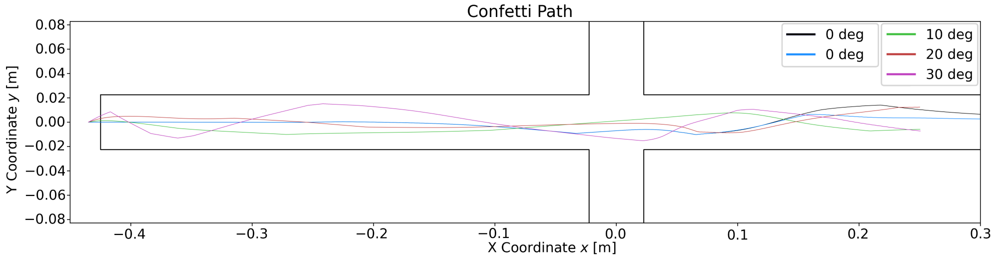

(b) Rotation around Y axis

Figure 5.24: Simulated trajectories, separated by offset rotation for confetti 1.

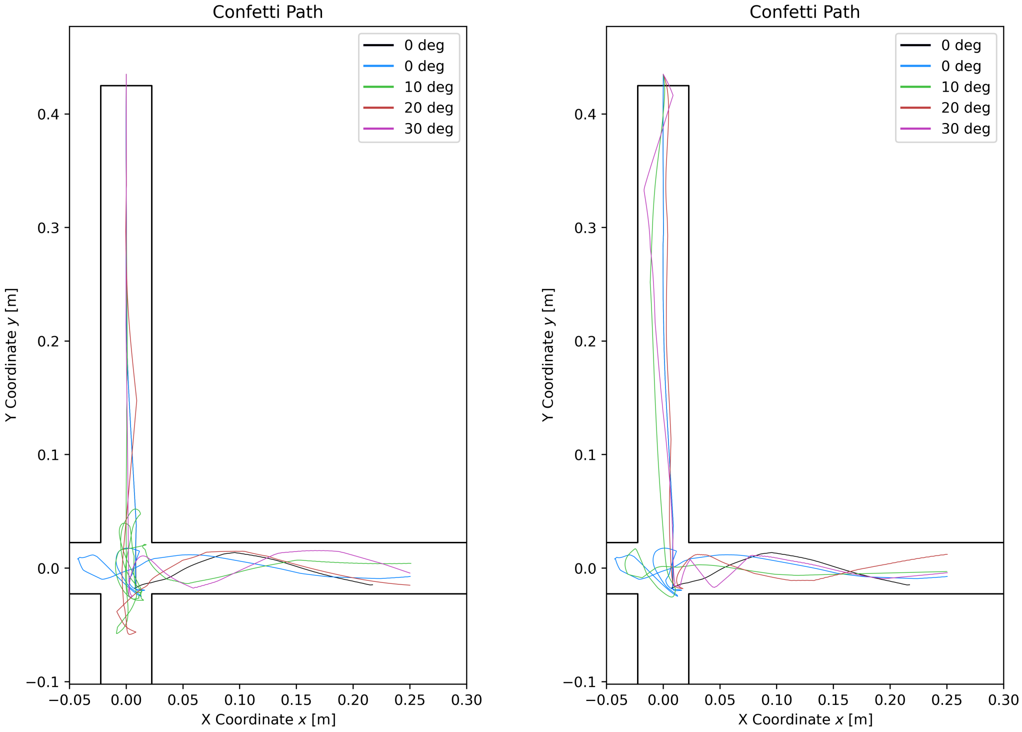

(a) Rotation around X axis

(b) Rotation around Z axis

Figure 5.25: Simulated trajectories, separated by offset rotation for confetti 2.

These results are not unexpected as when confetti is rotated, it encounters the flow unevenly with flow being deflected along its surface. In return, an aerodynamic force is exerted in the opposite direction, deflecting the confetti. With a larger angle, the force becomes greater with an increased deviation in trajectories. When not rotated, the force will most likely be facing the direction of travel due to initially symmetrical flow conditions. Only when rotation is initialized by changing flow conditions or contact, it starts to deviate from the center.

5.3.3 Positions

With simulations, all outputs share a known temporal reference frame and result in more accurate transient quantities. Now accounting for a third dimension, the total traveled dimension can be plotted and split by rotation as with figure 5.26. All have a gradually increasing velocity (slope) as they are captured by the flow, followed by relatively constant velocity in the inlets, switching to larger velocities when entering the outlet.

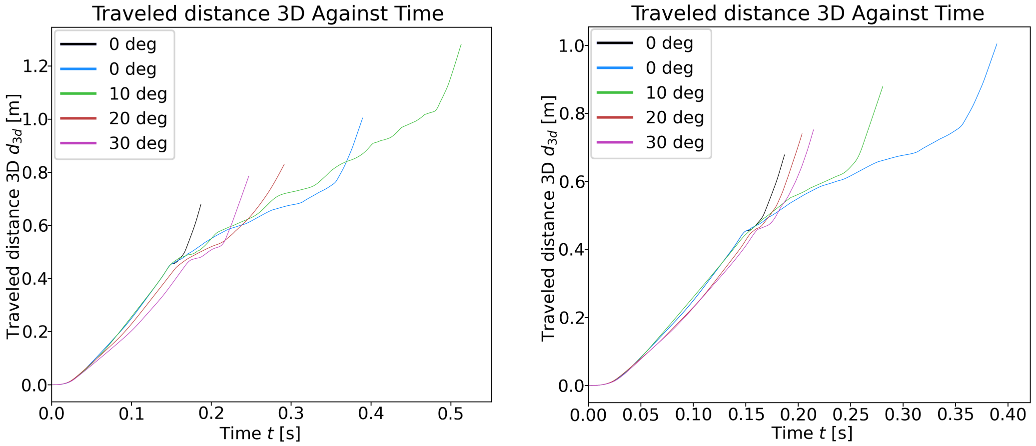

(a) Confetti 1, rotation X axis.

(b) Confetti 1, rotation Z axis.

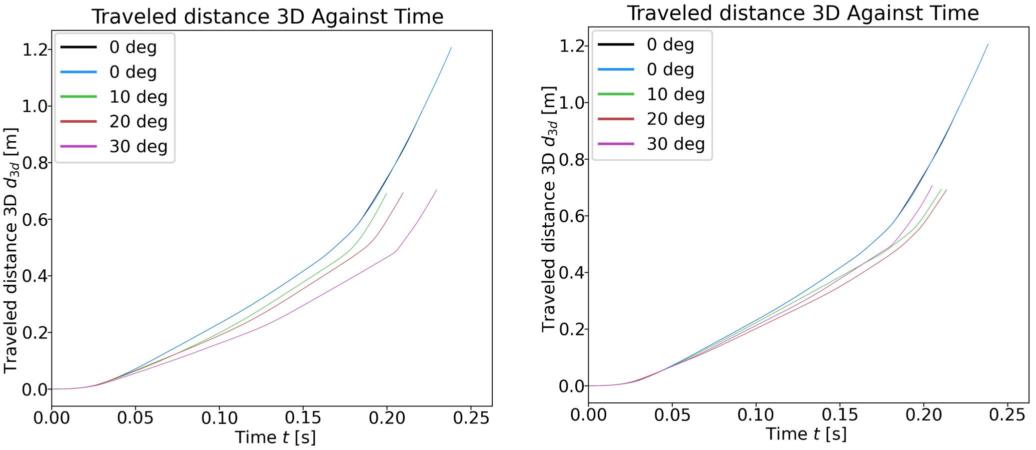

(c) Confetti 2, rotation Z axis.

(d) Confetti 2, rotation Y axis.

Figure 5.26: Total traveled distance against time, by confetti and rotation axis.

Looking specifically at the top row representative of confetti 1, there is an additional plateau region as confetti lingers in the junction. The offset angles seem unrelated to confetti lingering and are more likely decided by the numerical inconsistency. This is because the two identical, not rotated confetti, result in both the fastest and slowest transport as seen in figure 5.26b. In the same figure, both 10- and 20-degree offset linger longer than the 30-degree offset confetti further substantiating the claim.

From the bottom row with confetti one, no such plateau region exists, since no confetti lingers in the junction. Also seen in the trajectories in figure 5.24. These all have the three distinct regions mentioned earlier. Apart from the 30-degree offset in figure 5.26d, all are ordered with increasing angles related to smaller velocities slopes before the junction. While it indicates a correlation of offset rotated confetti having slower velocities in the inlets, this can not be concluded due to uncertainties present for confetti 1.

5.3.4 Velocities

The velocities are extracted from the confetti center again by finite difference of its coordinates. Without the human inaccuracies in positional data, the smoother trajectories result in smoother velocity transients, as seen for the four cases of not rotated confetti in figure 5.27.

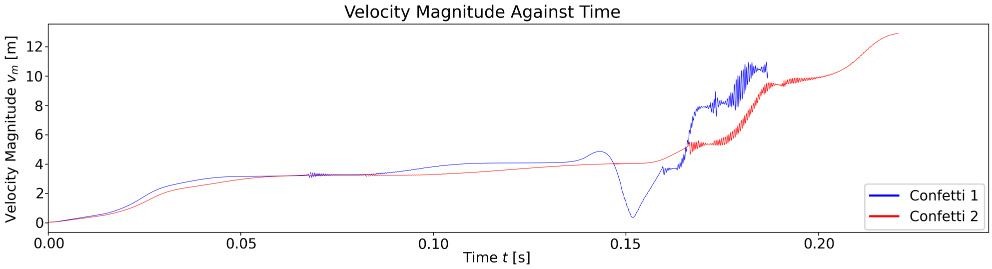

(a) First simulations.

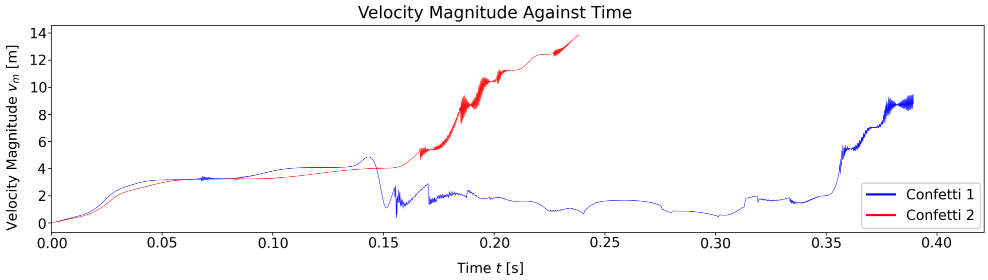

(b) Second simulations.

Figure 5.27: Velocity magnitude over time for confetti not rotated.

Unfortunately, there are still oscillations present, especially towards the end of the transients where there is also significant acceleration. As to why these occur, the first observable oscillation for confetti 1 of figure 5.27a is investigated further. At approximately 0.07 seconds, small oscillations are introduced to the otherwise smooth velocity transient. Unsurprisingly, this is the time of its first contact, indicated by the contact gap minimum of DP 1 in figure 5.22a which also has oscillations following contact.

Continuing the comparison of the same simulation, there is more contact at 0.14 and 0.15 seconds which does not produce oscillations. However, they are followed by repeated contact which initializes and amplifies oscillations from 0.16 seconds until the end. When further comparing figures 5.22 and 5.27, it is observed that oscillations are always initialized by contact, with larger oscillations related to repeated contact within smaller time frames.

One possible explanation is that the confetti is excited into an oscillating structural response by the contact impulse. Depending on the point of contact, a different response is initialized, possibly amplified by following contact impulses. Dampening is made by interaction with the surrounding air, as the material has no dampening model. However, more investigation is needed to determine the cause.

The smoother velocity profiles are observed in figures 5.28 and 5.29. Both illustrate the smooth trajectories with smooth velocity gradients with small oscillations. All confetti is shown to accelerate through both the inlet and outlet, differing in the junction where confetti 1 is stopped or lingers, while confetti 2 continues to accelerate. No visible decrease in velocity is seen when in contact with side walls.

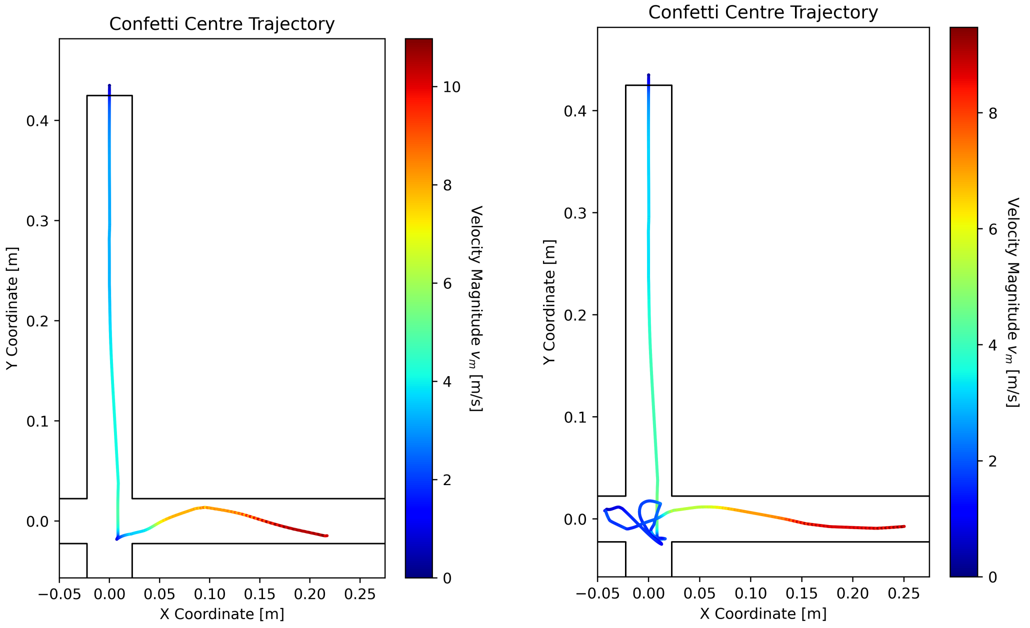

(a) Simulation one.

(b) Simulation two.

Figure 5.28: Velocity magnitude over trajectory for confetti 1. Both simulations without initial rotation with double-precision.

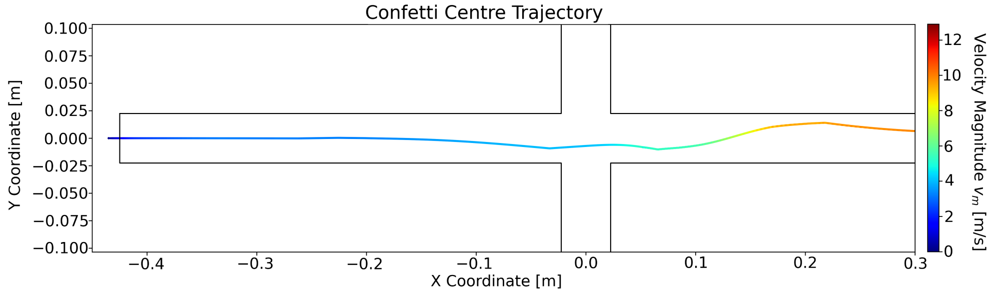

(a) Simulation one.

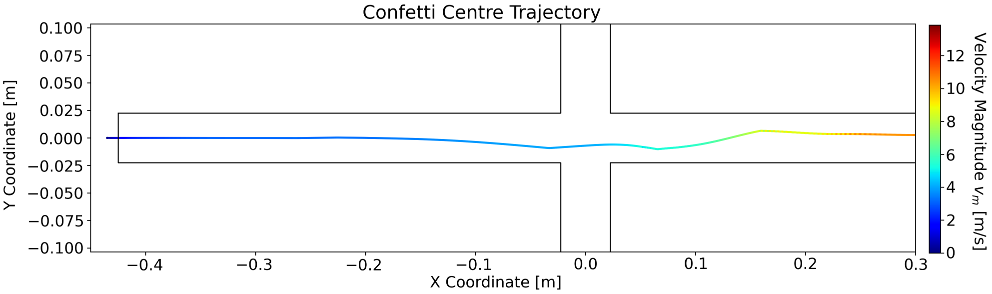

(b) Simulation two.

Figure 5.29: Velocity magnitude over trajectory for confetti 2. Both simulations were without initial rotation with double-precision.

The regions of interest defined in figure 5.23 are used again to calculate regional velocity averages. The average of each simulation is presented in figure 5.30 with all region averages in green.

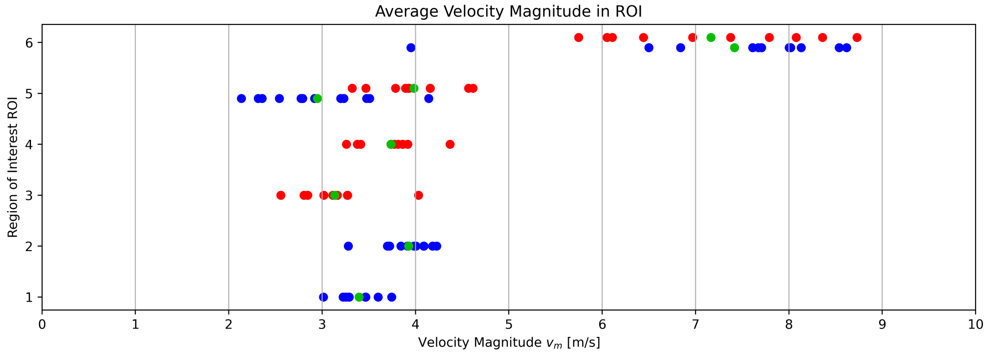

Figure 5.30: Velocity magnitude averages for simulations of confetti 1/2(blue/red) with overall region average (green).

Considering region 1 and 3 in the inlet middles, these show a small spread with confetti 1 having a larger region average velocity. Downstream in region 2 and 4, before the inlet, both have accelerated with larger region average velocities, compared to region 1 and 2. Still, confetti 1 is shown as faster and the spread is similar.

In the junction region 5, the spread for confetti 1 increases while the region average speed decreases compared to previous region 3. On the contrary, confetti 2 still gains region average velocity with no significant increase in spread. For the last region 6, all region averages are significantly larger than the others, but with an even larger spread.

5.3.5 Solver Diagnostics

For insight into the solver procedure, some key quantities are presented for only one confetti 2 simulation. It took 6,900 CPU hours to compute one simulation, corresponding to 44 hours of clock time. Comparatively, the longest confetti 1 simulation took 86 hours of clock time. For initialization, 180 GiB of memory was used which increased steadily to 220 GiB during confetti transport.

The time step size over time is illustrated in figure 5.31a. During initialization, the initial time step of 5 ms is used. During simulations, the adaptive time step was quickly changed from 5 to below 1 ms, where it often assumed the minimum value of 0.5 ms. It indicates that the time step is not sufficiently small for the target displacement, but it is still used to avoid even longer simulation times.

Average and maximum non-dimensional wall distances y^+ over time are illustrated in figure 5.31b. By its maximum value, it is shown that for most of the simulation, a low-y^+ wall treatment is used as $y^+ < 5$ for all cells. Only going above it briefly towards the end, the average indicates that most cells still receive a low-y^+ wall treatment. This indicates that the boundary layers are almost always resolved, avoiding wall functions.

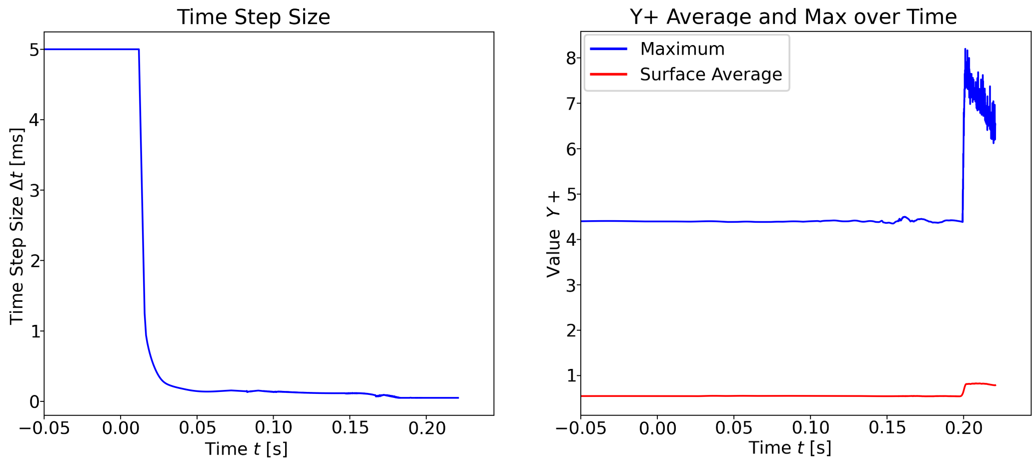

(a) Time step size over time.

(b) Average and maximum y^+.

Figure 5.31: Solver diagnostics, time step size and y^+.

5.4 Comparison

With results for both experiments and simulations, need to be compared. Confetti transport is indicated as chaotic by experiments, which can explain that simulations start to differ when a slight difference is initialized by contacts. Because of this, the primary comparison will be of the velocity averages. Trends in trajectories will also be compared.

5.4.1 Trajectories

In the comparison of trajectories, experimental and simulated confetti 1 are plotted in figure 5.32. At the inlets, the experiments quickly disperse while all simulated confetti remains relatively centered. This holds true until the junction, where both have some confetti entering the opposite inlet. The simulated confetti also enters the perpendicular inlet twice. In the outlet simulated confetti became more evenly distributed, similar to the experiments.

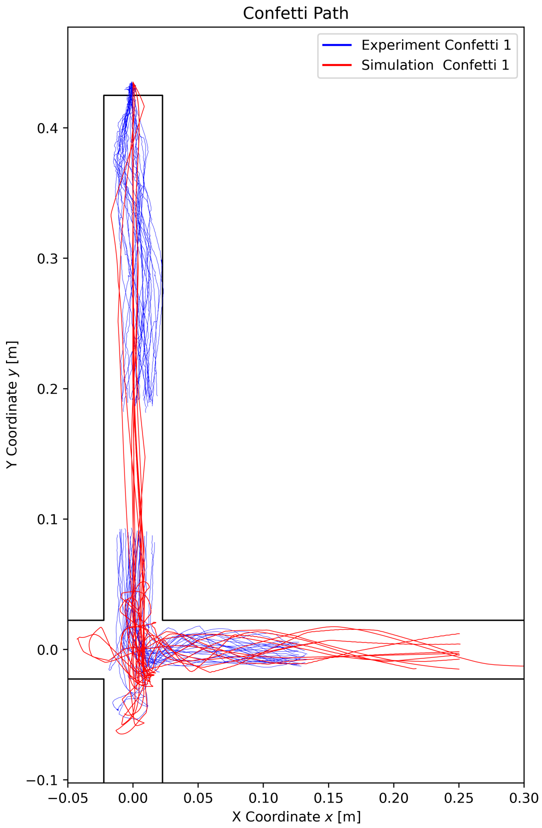

Figure 5.32: All confetti 1 trajectories from both simulations and experiments.

Comparisons for confetti 2 are made with figure 5.33, in which simulated confetti is again more centered initially. Further downstream near the inlet, they are dispersed like the experimental confetti. No confetti lingers in the junction but passes through it directly.

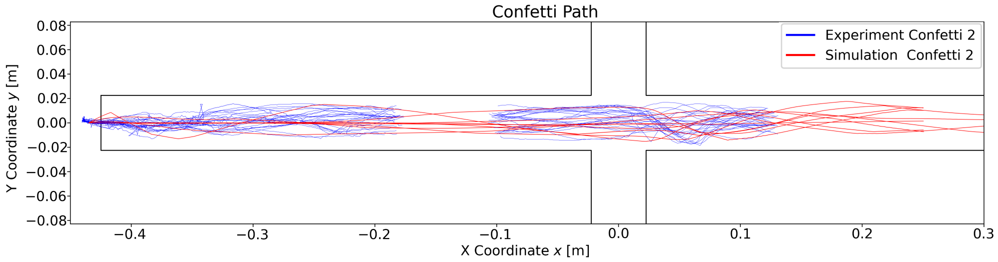

Figure 5.33: All confetti 2 trajectories from both simulations and experiments.

Observed in both figures, is that the experimental trajectories are less smooth. Its mild zigzagging trajectories are likely due to imprecise markings, or turbulent flow conditions within the pipes. Additionally, the quick dispersion of experimental confetti is likely related to an uncontrollable offset release angle, much like their simulated counterpart. Imperfect release of confetti was observed by the pneumatic release mechanism, which had an unreliable delayed release which also did not guarantee confetti being perpendicular to the pipe inlet.

5.4.2 Velocities

The two figures of average velocities, 5.19 and 5.30, are combined into a new figure 5.34 for an easier comparison. Directly, one observes that the region averages (green) are all larger for the simulated confetti, except for region 5, where they are almost identical. Also, almost all ranges of averages are smaller for simulations.

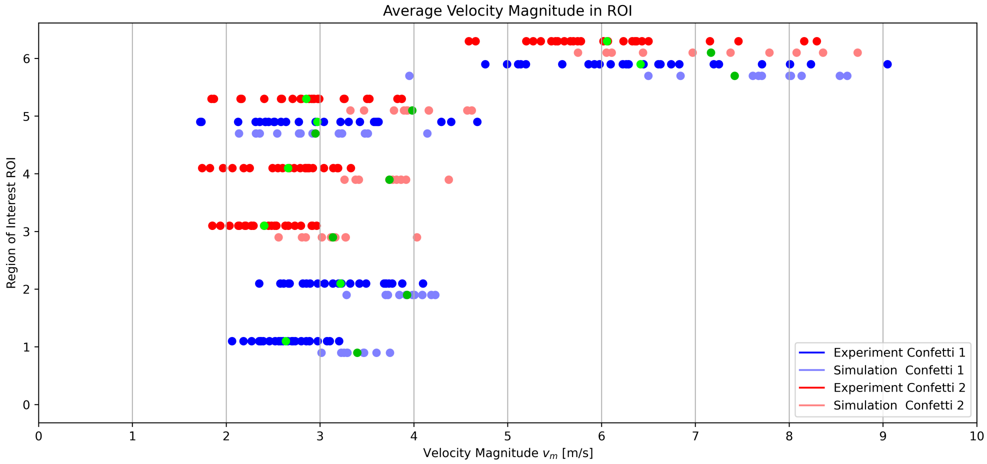

Figure 5.34: Velocity magnitude averages for simulations of confetti 1/2(blue/red) with overall region averages (green) for both experiments (dark) and simulations (light).

Addressing the first observation of simulations overestimating velocities, between 0 to roughly 1 m/s representing at most a roughly 50 % overestimation. Suspicions are again directed towards the contact model. In the discussion of paths with overlaid velocity, experiments illustrated a loss of velocity during contact with pipe walls, not seen in the simulations. These could be related to the observed electrostatic attraction or friction, neither of which are modeled by the contact model. Another possibility is that outlet mass flow has been improperly set due to faulty measurements.

It should be noted that the overestimation might be even larger due to the mild zigzagging in experimental trajectories. This zigzagging can inflate velocity estimations because it makes the trajectories longer than they are in reality. At the same time, the trajectories should be longer because positional data in the Z-axis are not recovered from experiments. Therefore, while the zigzagging might inflate the estimated velocities, the lack of Z-axis data could counter this by underestimating the true velocities.

The second observation, that the range of velocity averages is smaller for simulations, is attributed to the smaller sample size. With more experiments, it is more likely to capture outliers that are further from others. Also, multiple simulations are initially identical with differing trajectories only after contact, leading to many similar predictions and smaller ranges in the inlets. A more statistical approach would be to use variance and confidence intervals. However, it seemed unsuitable for the small sample size available.

Apart from these observations, it is noted that both simulations and experiments show that velocities become increasingly larger further downstream, apart from confetti 1 which slows down and lingers in the junction, also corresponding to a simultaneous increase in range.

5.4.3 General Observations

Comparing the discussion of experiments and simulations, further observations can be made. The small velocity oscillations present in the simulations are too small to be resolved by the experiments. To tell if the confetti vibrations are realistic, they must be studied more closely in experiments.

While confetti getting stuck was only observed once by experiments, it remains unanswered if the same can occur in simulations. From experience with contact model tests, the confetti never came to full rest but bounced around in the pipe with low intensity. Indicating that a resting and stuck confetti might be hard to capture.

The robustness of the models was good, but not perfect. During the 20 simulations, two had to be rerun due to unexpected crashes. Its efficiency was sufficient for the thesis analysis but could have been better, allowing for more simulations. A predecessor model performed well with only a sixth of the cells, indicating that more mesh optimization could be made in conjunction with a mesh sensitivity study.

6 Conclusion

In conclusion, the project successfully achieved its primary objectives of developing a new simulation model and conducting experiments for validation. The model was derived from a total of twenty models, ending with a single confetti simulation using a calibrated contact model with an overset mesh method for motion. It was used to simulate a total of twenty cases of confetti transport. The experiment led to the development of computer vision data extraction tools, which in conjunction with improved recording techniques, were used to extract data from a hundred experiments. Key findings from both are presented beneath.

6.1 Key Findings

All experimental trajectories indicated that confetti transport is chaotic as each confetti took unique paths, initialized by small uncontrollable differences from their release. With chaos, identical simulations with increased numerical precision were shown to differ over time, as small differences were introduced by the contact model.

Experimental trajectories were less smooth than their simulated counterpart since imperfect data extraction led to zigzagging trajectories. While experimental trajectories quickly become evenly distributed within the pipe width, simulated trajectories stay centered due to their more controlled initial conditions, also becoming evenly dispersed further downstream.

For a more conclusive evaluation of accuracy, regional trends in velocities were used to compare simulations against experiments. From this, it was observed that velocities always increase downstream, with one exception. Confetti entering from inlets orthogonal to the outlet, slowed down and lingered at the junction. However, in comparison of the overall averages over multiple simulations and experiments, the simulations always overpredict velocities. This is likely the result of either; unaccounted electrostatic attraction, imperfect contact without friction, or improper outlet velocity measurements. With corrections for trajectory zigzag from experiments, the overestimation becomes even higher.

In summary, chaotic confetti transport is impossible to predict accurately. A likely trajectory is simulated and is similar to experiments, but no simulation or experiment can be replicated identically. The overestimation of velocity is concerning, especially at inlets where they are the largest. While not perfect, the models still serve as a new tool for further development at Tetra Pak, with many suggestions for improvement included in the following Future Work section.

6.2 Future Work

This thesis was limited in its scope and explored alternative approaches, not all presented here. Based on learnings throughout the thesis and of the imperfect last model, there is a potential for improvements. More work can be done to improve both the simulation models and the validation process containing the recording and extraction of data.

6.2.1 Experiments

The conclusion that confetti transport is inherently chaotic, is problematic for the study of it. While a decent dataset was gathered and analyzed for trends, it is a relatively small sample size. For more statistically accurate conclusions, more data is needed. While experiments are performed with relative ease, inefficient data extraction limits the scope of these efforts.

There is already another set of a hundred recordings that have yet to be analyzed. These were of same-sized confetti with a slightly different material composition. Meant for a study of the impact of materials, these were abandoned due to time restrictions, but are available for a future analysis. However, with such similar conditions to already analyzed confetti, it is likely to require even more recordings to make a good comparison.

Suggested improvements for the data extraction are based on better recording techniques and more advanced computer vision scripting. Obstructions per figure 3.6c could be addressed by joining the acrylic pipes by different techniques, to eliminate overlaps and air bubbles. Light could also be diffused more efficiently to avoid harsh reflections and bright virtual confetti as in figure 3.6b.

Higher-resolution high-speed cameras could be utilized alongside wider lenses, to capture both inlets and the junction simultaneously. This would fill gaps between data sets, producing continuous experimental trajectories. Such cameras are available at Tetra Pak, even with color capture. With colored confetti and footage, identification amongst multiple confetti becomes possible with better potential for filtering.

While previous work determined that plastic deformation was unnecessary for confetti transport, it is unknown to which extent confetti is deformed or if it oscillates after contact as suggested by simulations. Experiments that closely study confetti during contact could inform new model requirements or simplifications. For instance, a damping model could be added or deformation could be removed entirely.

A lot of work went into the development of computer vision scripting, being updated many times in conjunction with new recording techniques. Considering it was not the main objective of the thesis and with diminishing returns to the time invested, development was paused when its utility was good enough. As a compromise, markings were not always accurate and required human markings, which apart from taking time were to some extent also inaccurate. Development of a fully automated and more accurate computer vision script or program, could itself be a thesis. Suggestions for improvements are the use of computer vision trackers, which can utilize context from history and be trained to identify confetti by machine learning.

Still, even with all these improvements, there is yet another limitation to the experiments. While confetti entering opposite pipes was captured often, only one of two hundred experiments had a confetti get stuck. Most of the time, extraction works as intended and to capture the cases when they don't might require many more experiments.

6.2.2 Simulations

In terms of the simulation model, four key properties are evaluated for improvements: accuracy, robustness, efficiency, and complexity. Beginning with accuracy, a better evaluation could only be made if more samples were available for a more rigorous statistical analysis. Additionally, it should be investigated if numerical inconsistency could be reduced further or even removed. For example, by decreasing the time step size, using more stringent convergence criteria, and by adjusting the contact model.

The robustness of the model was sufficient for this thesis, but it still crashed one out of ten times. As they occur unexpectedly only the aftermath was available for investigation, which mostly show negative cells with confetti close to walls. Previous models suggested that an increase in contact gap offset in the contact model could increase robustness but at a possible expense of accuracy. Similar issues but more frequent, contributed to the abandonment of models with multiple confetti.

Considering the cost, the current mesh is fine in relation to the optimized meshes of predecessor general remeshing models which used only a sixth of the current cell count. A more controlled meshing with regional refinement at the junction, and coarser inlet extensions, the mesh could be further optimized. Considering that the four arms and corresponding flow are largely aligned with the coordinate axes, a structured hexahedral mesh could increase the efficiency. Further, the mesh choice should be evaluated by a mesh sensitivity study. If the result is a lower cost, more simulations can be run to make better statistical evaluations.

Regarding complexities, the final model could not handle multiple confetti which did work at one point during the development process. However, it was abandoned due to confetti-confetti contact which caused poor robustness and was not supported by simulation software providers. If confetti-confetti contact is avoided, the model might be able to handle multiple confetti simultaneously. One way to avoid unwanted contact is to release confetti unsynchronized, like the imprecise release mechanism of the experiments.

A significant limitation of the RANS model is its inability to resolve turbulent effects. This is particularly crucial for particle flows, similar to confetti transport, where local fluctuations or eddies can significantly impact their behavior and transport. The flow within the pipe may not be steady as in the simulations. Hence, flow conditions within the pipe should be evaluated with smoke to provide insight into the presence of turbulent fluctuations which might not be captured by the currently used RANS model.

6.2.3 Rotary Die Cutter Model

While this thesis has advanced the modeling of confetti transport at Tetra Pak, the model is still not capable of replicating some complexities of the real rotary die cutter. The ultimate goal at Tetra Pak is to model a rotating system with more inlets, higher velocities, and a greater number of interacting confetti. Achieving this goal will require improved capabilities of the simulation software, as well as further development of exploratory models at Tetra Pak.

Bibliography

[1] T. Richter. *Fluid-structure Interactions*. Springer, 2017. ISBN: 9783319639703. DOI: `https://doi.org/10.1007/978-3-319-63970-3`.

[2] Tetra Pak. *About Tetra Pak*. 2023. URL: `https://www.tetrapak.com/about-tetra-pak`. (accessed: 2023-12-11).

[3] L. Christierson. *The Investigation and Modeling of the interaction between Paperboard Clippings in a Pipe Flow*. Lund University Publications Student Papers, 2021. URL: `http://lup.lub.lu.se/student-papers/record/9040215`.

[4] P.M. Gerhart, A.L. Gerhart, and J.I. Hochstein. *Munson's Fluid Mechanics*. Singapore, SG: John Wiley & Sons, 2017. ISBN: 9781119248989.

[5] H.K. Versteeg and W. Malalasekera. *An Introduction to Computational Fluid Dynamics*. Harlow, UK: Pearson Education Limited, 2007. ISBN: 9780131274983.

[6] J.D. Anderson Jr. *Fundamentals of aerodynamics*. New York, NY: McGraw-Hill Education, 2011. ISBN: 9781259010286.

[7] E.B. Tadmor, R.E. Miller, and R.S. Elliott. *Continuum Mechanics and Thermodynamics*. Cambridge, UK: Cambridge University Press, 2012. ISBN: 9781107008267.

[8] S.B. Pope. *Turbulent Flows*. Cambridge, UK: Cambridge University Press, 2003. ISBN: 9780521598866.

[9] Siemens Digital Industries Software. *Simcenter STAR-CCM+ 2310 User Guide*. 2023. URL: `https://cloud.sw.siemens.com/starccmviewer/70f6faed-c328-471e-83b0-e54c93451165/WebViewerHelp.pdf`.

[10] N. Saabye Ottosen and M. Ristinmaa. *The mechanics of constitutive modeling*. Oxford, UK: Elsevier Science Ltd, 2005. ISBN: 9780080446066. DOI: `https://doi.org/10.1016/B978-0-08-044606-6.X5000-0`.

[11] N. Ottosen and H. Petersson. *Introduction to the Finite Element Method*. Harlow, UK: Pearson Prentice Hall, 1992. ISBN: 9780134738772.

[12] J.H. Ferziger, M. Perić, and R.L. Street. *Computational Methods for Fluid Dynamics*. Springer, 2020. ISBN: 9783319996936. DOI: `https://doi.org/10.1007/978-3-319-99693-6`.

[13] R.K. Jaiman and V. Joshi. *Computational Mechanics of Fluid-Structure Interaction*. Springer, 2021. ISBN: 9789811653551. DOI: `https://doi.org/10.1007/978-981-16-5355-1`.

Appendices

A Populärvetenskaplig Sammanfattning

Att simulera transporten av kartong-konfetti i rör

av Ludvig Willemo

Tetra Pak är ett globalt livsmedels- och förpackningsföretag, bäst känt för sina hållbara kartongförpackningar som tillverkas i miljarder vart år. Många sådana förpackningar kräver hål för korkar och sugrör, vilket leder till ytterligare miljarder av konfetti-liknande kartongrester. Dessa konfetti måste tas bort från maskinerna för att de ska fungera felfritt. För att garantera detta studeras transporten av konfetti genom både verkliga experiment och virtuella datorsimuleringar, vilket bidrar till utvecklingen av pålitliga utsugningssystem.

Experimenten görs med ett genomskinligt fyrvägsrör genom vilket luft sugs av ett vakuumsug. När konfetti släpps ut vid ett av de tre inloppen passerar det snabbt igenom systemet under bråkdelen av en sekund. Förloppet är för snabbt för att kunna ses med blotta ögat! I stället används en höghastighetskamera för att fånga vad som sker, flera gånger om. En dator är programmerad att därefter hitta konfetti i varje inspelning och spara varje väg som de tar genom röret.

Simuleringar görs med modeller som återskapar experimenten i en virtuell miljö. Rörets geometri kopieras och delas upp i två områden, som var för sig representerar luft samt konfetti och tilldelas motsvarande fysiska egenskaper. En uppsättning komplexa ekvationer, formulerade utifrån fysikaliska lagar, anger hur luftflödet och konfettin ska förändras. För att lösa ekvationerna delas luftområdet upp i miljontals små delar, på vilka enklare ekvationer kan användas. Med information från närliggande delar och historiska värden utvärderas alla delar separat. När alla delar sedan sätts ihop resulterar det i ett flöde som kan flytta konfettin. Med tusentals upprepningar återskapas transporten av konfetti långsamt under tre dagar med hjälp av en mycket kraftfull dator.

I både virtuella och verkliga experiment tog konfettin en ny väg genom röret varenda gång! Transportprocessen är till synes kaotisk; små initiala skillnader kan leda till betydande skillnader i vägen som tas. Om man jämför modeller med experiment är banorna liknande, men ofullständiga simuleringar förutspår för stora hastigheter.

Med kaotiska egenskaper är det omöjligt att exakt förutspå individuella konfettibanor och hastigheter. Men med statistik från flera simuleringar kan modellen approximera trender för konfettitransport liknande de resultat som fås genom experiment. Liksom en väderprognos kan den inte förutspå den exakta placeringen av varje regnmoln, men den ger dig en ganska bra uppfattning om vad som kan förväntas. Även om den inte är perfekt kan Tetra Pak använda dessa modeller för att bättre förstå problem som uppstår när konfetti transporteras genom rör.

B Popular Science Summary

Simulating the Transport of Paperboard Confetti in Pipes

by Ludvig Willemo

Tetra Pak is a global food processing and packaging company, best known for their sustainable carton packages, which are produced by the billions each year. Many of these packages require holes for straws and caps, creating additional billions of confetti-like paperboard scraps. These confetti must be removed from the machines to keep them running smoothly. To ensure this, the transport of confetti is studied by both real-life experiments and virtual computer simulations, informing the design of reliable extraction systems.

Experiments are made with a see-through four-way pipe that has air sucked through it by a vacuum. When confetti is released at one of the three inlets, it quickly passes through the system during a fraction of a second. The process is too quick to observe with the naked eye! Instead, a high-speed camera is used to capture what happens, many times over. A computer is programmed to find confetti in each recording, saving every path that they take through the pipe.

Simulations are made with models that recreate the experiments in a virtual environment. The pipe geometry is copied and split into two regions, each representing air and confetti by assigning corresponding physical properties. A set of complex equations, formulated from a set of physical laws, states how airflow and confetti should evolve. To solve the equations, the air region is split into millions of tiny parts, on which simpler equations can be used. With information from neighboring parts and historical values, all parts are evaluated separately. When all parts are put together, it results in a flow that can move the confetti. Repeated thousands of times, confetti transport is slowly recreated over three days using a very powerful computer.

In both virtual and real experiments, the confetti took a new path through the pipe every single time! The transport process is seemingly chaotic; small initial differences can lead to significant variations in the path taken. Comparing models to experiments, trajectories are similar but imperfect simulations that predict too large velocities.

With chaotic traits, it is impossible to accurately predict individual confetti trajectories and velocities. However, with statistics from multiple simulations, the model can approximate trends of confetti transport that are similar to results obtained by experiments. Akin to a weather forecast, it does not predict the exact location of each rain cloud, but it gives you a fairly good idea of what to expect. While not perfect Tetra Pak can use these models to better understand issues arising from confetti being transported through pipes.